Eur. J. Mineral., 35, 479–498, 2023
https://doi.org/10.5194/ejm-35-479-2023

European Journal of Mineralogy
Open Access

Detrital garnet petrology challenges Paleoproterozoic ultrahigh-pressure metamorphism in western Greenland

Jan Schönig[1], Carsten Benner[1], Guido Meinhold[2], Hilmar von Eynatten[1], and N. Keno Lünsdorf[1]

[1]Department of Sedimentology and Environmental Geology, Geoscience Center Göttingen, University of Göttingen, 37077 Göttingen, Germany
[2]Institute of Geology, TU Bergakademie Freiberg, 09599 Freiberg, Germany

Correspondence: Jan Schönig (jan.schoenig@uni-goettingen.de)

Received: 7 March 2023 – Revised: 9 June 2023 – Accepted: 12 June 2023 – Published: 17 July 2023

Abstract. Modern-style plate tectonics is characterised by the global operation of cold and deep subduction involving blueschist facies and ultrahigh-pressure metamorphism. This has been a common process since the Neoproterozoic, but a couple of studies indicate similar processes were active in the Paleoproterozoic, at least on the local scale. Particularly conspicuous are extreme ultrahigh-pressure conditions of ~ 7 GPa at thermal gradients $< 150\,^{\circ}\mathrm{C\,GPa^{-1}}$ proposed for metamorphic rocks of the Nordre Strømfjord shear zone in the western part of the Paleoproterozoic Nagssugtoqidian Orogen of Greenland. By acquiring a large dataset of heavy minerals ($n = 52\,130$) and garnet major-element composition integrated with mineral inclusion analysis ($n = 2669$) from modern sands representing fresh and naturally mixed erosional material from the metamorphic rocks, we here intensely screened the area for potential occurrences of ultrahigh-pressure rocks and put constraints on the metamorphic evolution. Apart from the absence of any indications pointing to ultrahigh-pressure and low-temperature–high-pressure metamorphism, the results are well in accordance with a common Paleoproterozoic subduction–collision metamorphic evolution along a Barrovian-type intermediate temperature and pressure gradient with a pressure peak at the amphibolite–granulite–eclogite-facies transition and a temperature peak at medium- to high-pressure granulite-facies conditions. In addition, we discuss that all "evidence" for ultrahigh-pressure metamorphism proposed in the literature for rocks of this area is equivocal. Accordingly, the Nordre Strømfjord shear zone is not an example of modern-style plate tectonics in the Paleoproterozoic or of very low thermal gradients and extreme pressure conditions in general.

1 Introduction

Plate tectonics is the global-scale horizontal movement of tectonic plates (e.g. McKenzie and Parker, 1967) driven by the sinking of cold and dense oceanic lithosphere into the mantle (e.g. Forsyth and Ueda, 1975). Because plate tectonics is a prerequisite for recycling large volumes of surface materials into the mantle via subduction (e.g. Hawkesworth et al., 2016), tracking the operation of plate tectonics through time has profound implications for the understanding of Earth's long-term evolution (e.g. Palin et al., 2020). Geodynamics of the Earth probably evolved from a pre-plate-tectonic to a plate-tectonic regime, whereby the transitional time interval is called the onset of global subduction (e.g. Dhuime et al., 2012). Its placement onto the geological timescale is one of the most controversial topics in Earth sciences. Most point to a Mesoarchean onset (e.g. Brown et al., 2020; Palin et al., 2020), but afterwards the Earth's geodynamic regime may have switched between episodes of non-plate tectonics and plate tectonics (Stern, 2023; Salminen et al., 2023).

Whether plate tectonics developed rapidly, slowly, or episodically to the modern-style regime, which is characterised by cold and deep subduction (i.e. blueschist and ultrahigh-pressure metamorphism), is a matter of debate, particularly because the metamorphic record is skewed by overprinting and erosion (e.g. Cawood et al., 2013; Weller and St-Onge, 2017). This is obvious considering metamorphic temperature and pressure gradients through time (Brown, 2006;

Brown and Johnson, 2018), which show that the majority of data correspond to Phanerozoic rocks and those of Precambrian age are subordinate (Fig. 1, blue kernel density estimate map). By using locally estimated smoothing, an abrupt decrease in temperature and pressure gradients is observed from the Neoproterozoic onwards (Fig. 1, red line), while data binning regarding distinct age populations indicates an increasing bimodality of gradients with decreasing age, interpreted as indicating secular cooling since the earliest Paleoproterozoic (Holder et al., 2019; Fig. 1, density curves). Notably, low-temperature and low-pressure metamorphic conditions are observed for a number of Paleoproterozoic rocks in different regions worldwide (Fig. 1; Ganne et al., 2012; Glassley et al., 2014; Perchuk and Morgunova, 2014; Weller and St-Onge, 2017; François et al., 2018; Xu et al., 2018; de Oliveira Chaves and Porcher, 2020). Whether these indicate a global modern-style plate-tectonic network or local modern-style subduction zones that are non-representative of the dominant tectonic regime is debatable (Brown and Johnson, 2019).

The earliest unequivocal evidence for blueschists and coesite-bearing supracrustal ultrahigh-pressure rocks is of Neoproterozoic age, i.e. ~ 800 and ~ 611 Ma, respectively (Maruyama et al., 1996; Jahn et al., 2001; Ganade et al., 2023). A significant outlier in this context is given by the Paleoproterozoic (~ 1.8 Ga) ultrahigh-pressure event with extreme conditions of ~ 985 °C and ~ 7 GPa proposed for Mn-rich ultramafic and quartzo-feldspathic rocks in the Nordre Strømfjord shear zone of the western part of the Nagssugtoqidian Orogen in Greenland (Glassley et al., 2014; Fig. 1). These pressure–temperature estimates are based on (1) oriented chlorine-bearing hydrous mineral inclusions, interpreted as being a phase replacing former orthopyroxene and thus implying orthopyroxene exsolution from a majoritic garnet precursor; (2) inclusions containing carbonaceous matter, interpreted as diamond partially replaced by graphite; (3) oriented rutile inclusions in garnet and clinopyroxene as well as oriented and complex clinopyroxene–orthopyroxene features, interpreted as exsolution subsequent to ultrahigh-pressure metamorphism; and (4) oriented quartz inclusions in fayalitic olivine, interpreted as exsolution from an ahrensite (Fe_2SiO_4) precursor (Glassley et al., 2014, 2016). If correct, these rocks not only represent Earth's oldest supracrustal ultrahigh-pressure rocks but also show the lowest metamorphic gradients and highest-pressure conditions in the entire dataset of metamorphic rocks through time, together with rocks of the Phanerozoic Kokchetav massif (Katayama and Maruyama, 2009; Fig. 1).

To screen the Nordre Strømfjord shear zone for potential occurrences of ultrahigh-pressure rocks and to put constraints on the metamorphic evolution of the area, we here present the following: (1) a large dataset of detrital heavy minerals acquired by semi-automated Raman spectroscopy ($n = 52\,130$), (2) detrital garnet major-element chemistry acquired by electron microprobe analysis ($n = 2669$), and (3) mineral inclusion analysis of the detrital garnet grains by hyperspectral Raman imaging ($n = 2669$). Particularly, the analysis of mineral inclusions in detrital garnet is a powerful tool to detect the extent of eclogite-facies and ultrahigh-pressure metamorphic rocks by mineralogical evidence, relying on unequivocal indicator minerals like omphacite, coesite, and diamond (Schönig et al., 2022). This has been successfully applied in the Western Gneiss Region of Norway (Schönig et al., 2018a, b), the central Saxonian Erzgebirge (Ore Mountains) of Germany (Schönig et al., 2019, 2020, 2021a), and the D'Entrecasteaux metamorphic complex of Papua New Guinea (Baldwin et al., 2021). Our findings from the Nordre Strømfjord shear zone, apart from the lack of any indications of low-temperature–high-pressure and/or ultrahigh-pressure metamorphism, are in agreement with a Barrovian-type metamorphic evolution at an intermediate thermal gradient. Intermediate gradients are common in the majority of Mesoarchean–Mesoproterozoic subduction–collision zones but inconsistent with a supposed ultrahigh-pressure terrane formed in a modern-style deep and cold subduction regime.

2 Geological setting and samples

The Nagssugtoqidian Orogen is located in southern Greenland (Ramberg, 1948; Fig. 2a). It represents a west-northwest-striking orogenic belt, stretching from the western to the eastern coast. Orogenesis resulted from south-directed subduction and Paleoproterozoic (~ 1.87 Ga) collision of the southern North Atlantic Craton and the northern Rae Craton (e.g. Kalsbeek et al., 1987; Marker et al., 1995). The Nagssugtoqidian Orogen is covered to a great extent by the inland ice sheet but exposed at the western and eastern coasts.

In western Greenland, the orogen is subdivided into a northern, central, and southern orogen (Marker et al., 1995; Fig. 2b). The southern and central orogen are separated by the Ikertôq thrust zone – also called Ikertôq steep belt – and the boundary to the northern orogen is delineated by the Nordre Strømfjord shear zone – also called Nordre Strømfjord steep belt. Initial collision of the Archean cratons is recorded at ~ 1.85 Ga in the central orogen (Taylor and Kalsbeek, 1990; Kalsbeek and Nutman, 1996; van Gool et al., 1999; Connelly et al., 2000), accompanied by north-west-directed thrusting, crustal thickening, and granulite-facies metamorphic conditions (Davidson, 1979; Hansen, 1979; Glassley, 1983). Subsequently, collisional deformation progressed into the southern and northern orogen, peaking at ~ 1.78 Ga under mainly amphibolite-facies conditions, locally reaching the granulite facies (Glassley and Sørensen, 1980; Connelly and Mengel, 2000; Mazur et al., 2012). Simultaneously, the central orogen was affected by up to kilometre-scale collisional folding, followed by post-collisional large-scale folding and finally sinistral strike-slip shearing within the steep belts (Connelly et al., 2000; van Gool et al., 2002; Fig. 2b).

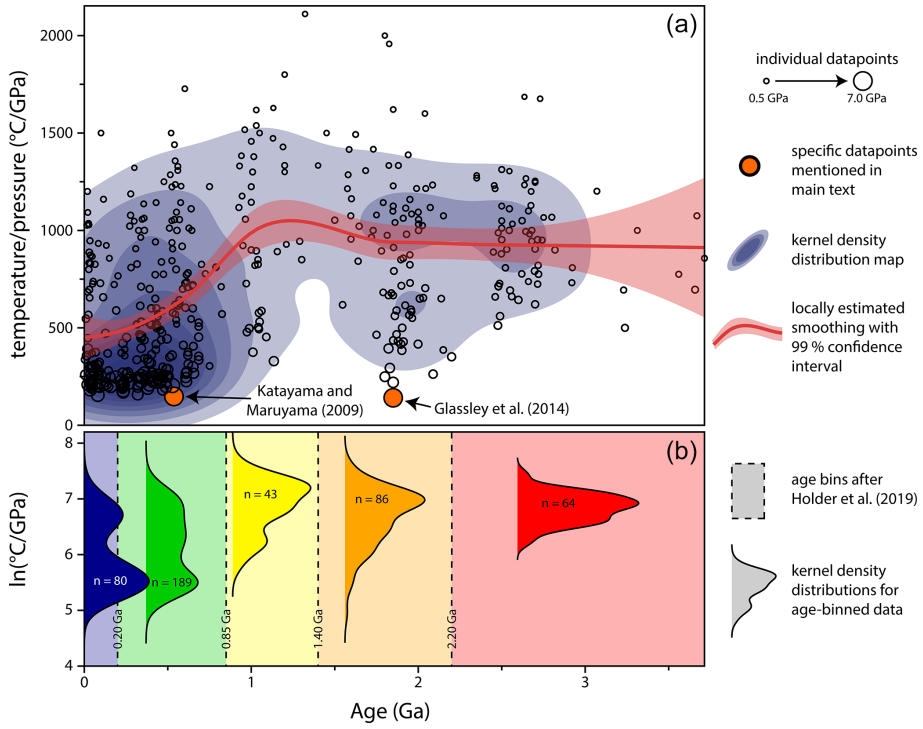

Figure 1. Temperature and pressure gradients of metamorphic rocks through time. Dataset from Brown and Johnson (2018, $n = 456$), extended by six observations from five Paleoproterozoic localities (Perchuk and Morgunova, 2014; François et al., 2018; Müller et al., 2018; Xu et al., 2018; de Oliveira Chaves and Porcher, 2020). Panel **(a)** shows data points of individual localities, a kernel density distribution map of the data distribution (Wickham, 2016) with bandwidth calculated after Venables and Ripley (2002), and a locally estimated scatterplot smoothing regression curve with 99 % confidence interval (Cleveland et al., 1992; R Core Team, 2021). Panel **(b)** shows kernel density estimate distributions for age-binned data after Holder et al. (2019); bandwidth calculated after Silverman (1986).

The study area is located in one of those steep belts, the Nordre Strømfjord shear zone, which marks the northernmost part of the central orogen (Fig. 2b). This shear zone is tilted to the east, resulting in a widening as well as an exposure of deeper crustal levels in the western direction (Bak et al., 1975; Glassley et al., 2010). Thermobarometric constraints for rocks in the study area and surroundings mainly indicate 700–900 °C and 0.6–1.0 GPa (Fig. 2b; Davidson, 1979; Hansen, 1979; Glassley, 1983; Mazur et al., 2012). In contrast, local eclogite-facies conditions of ∼ 785 °C and 2.1 GPa are proposed for a metasomatic reaction rim in an ultramafic lens (Glassley et al., 2007), and extreme ultrahigh-pressure conditions of 920–1045 °C and 5.9–8.0 GPa are inferred for ultramafic and quartzo-feldspathic rocks occurring in the study area (Glassley et al., 2014; Fig. 2c; see Sect. 1). The ultramafic ultrahigh-pressure rocks are Mn-rich, contain olivine + garnet + clinopyroxene + orthopyroxene + quartz ± graphite ± magnetite ± ilmenite, and are interpreted as ocean-floor exhalative metasediments (Glassley et al., 2014). Besides these scarce ultramafic lenses, the framework of the study area is mainly composed of granodioritic–tonalitic gneiss containing biotite + orthopyroxene + amphibole (hornblende) + garnet (Fig. 2c, yellowish colours), metasedimentary and/or metavolcanic rocks containing garnet + sillimanite + biotite ± graphite ± cordierite (brownish colours), metasedimentary and/or metavolcanic rocks containing biotite + pyroxene + graphite ± garnet ± cordierite (orangish colours), amphibolites containing garnet + clinopyroxene + orthopyroxene (green colour), granitic/charnockitic rocks that locally contain garnet (reddish colours), calc-silicate rocks (light blue colour), Quaternary deposits (light grey colour), and dispersed ultramafic lenses and pegmatite dikes (Olesen, 1984).

Modern sands from eight catchments draining the various lithologies, including proposed ultrahigh-pressure rocks, were sampled during fieldwork in August 2020 (Fig. 2c). Catchments of samples JS-NGO-01s, JS-NGO-03s, and JS-NGO-21s are mainly composed of tonalitic orthopyroxene-rich gneiss, particularly JS-NGO-03s. Samples JS-NGO-16s, JS-NGO-17s, and JS-NGO-18s are from catchments draining a section of intercalated graphite-bearing garnet–sillimanite–biotite schist/gneiss and amphibolites. Catchments of JS-NGO-09s and JS-NGO-11s are composed of similar proportions of orthopyroxene-rich gneiss, graphite-bearing garnet–sillimanite–biotite schist/gneiss, and biotite–pyroxene–graphite schist.

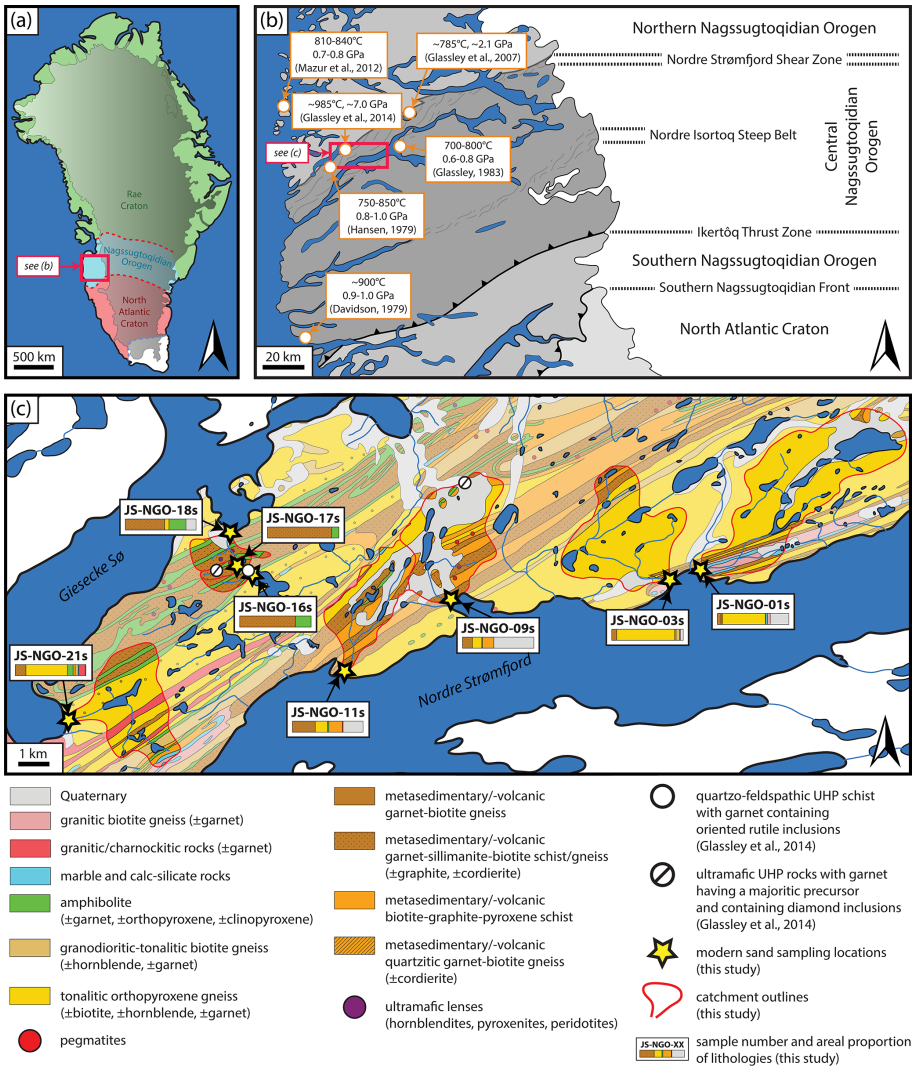

Figure 2. Geological setting and sampling locations. **(a)** Overview of Greenland showing the approximate outline of the Nagssugtoqidian Orogen modified from Escher and Pulvertaft (1995), van Gool et al. (2002), and St-Onge et al. (2009). **(b)** Structural units of the Nagssugtoqidian Orogen defined by Marker et al. (1995) and adopted from van Gool et al. (2002) and van Gool and Marker (2007). Pressure–temperature conditions for metamorphic rocks of the study area and surroundings are indicated. **(c)** Geological map of the study area located in the Nordre Strømfjord shear zone adopted from Olesen (1984). Modern sand sampling locations are as follows: JS-NGO-01s (67°47′18.20″ N, 52°39′37.50″ W), JS-NGO-03s (67°47′3.90″ N, 52°41′15.50″ W), JS-NGO-09s (67°46′43.70″ N, 52°51′47.10″ W), JS-NGO-11s (67°45′28.30″ N, 52°56′45.70″ W), JS-NGO-16s (67°47′12.90″ N, 53°01′19.80″ W), JS-NGO-17s (67°47′24.90″ N, 53°01′55.00″ W), JS-NGO-18s (67°47′45.90″ N, 53°2′30.20″ W), and JS-NGO-21s (67°44′31.30″ N, 53°10′5.20″ W).

3 Methodology

All sample preparation and analytical methods were performed at the Geoscience Center of the University of Göttingen.

3.1 Sample preparation

Sand samples were wet-sieved to extract three grain-size fractions: 63–125, 125–250, and 250–500 µm. The individual fractions were treated with low-concentrated acetic acid to remove the carbonate content if present, and the heavy-mineral fraction was separated by centrifugation using sodium polytungstate with a density of $\sim 2.89\,\mathrm{g\,cm^{-3}}$. Heavy-mineral concentrates were embedded in synthetic mounts using a bonding epoxy. Mounts were ground with silicon carbide abrasive paper and polished in five steps with Al_2O_3 abrasives in water suspension to a finest particle size of 0.05 µm.

3.2 Raman spectroscopy

3.2.1 Semi-automated heavy-mineral analysis

Following Lünsdorf et al. (2019), the polished mounts were photographed in reflected and transmitted light using a 20× objective (NA 0.45) and a Zeiss Axio Imager M2m microscope. Individual photographs were stitched to a mosaic, and measurement coordinates were defined for all grains of all samples and grain-size fractions (i.e. Fleet method; Fleet, 1926) using in-house-written software ("coordsetter"). The created x–y–z coordinate lists were transferred to a Horiba Jobin Yvon XploRA Plus Raman spectrometer equipped with an Olympus BX41 microscope and a motorised x–y–z stage. Measurement conditions include a 532 nm excitation laser (max output power 100 mW), a 1200 lines mm^{-1} grating covering a spectral range of 100–2800 cm^{-1} with a spectral resolution of $\sim 3.1\,cm^{-1}$, a 50× long-working-distance objective (NA 0.50), an automated exposure time estimated to reach 5000 counts for each individual grain analysis (max exposure time 20 s), and a reduced laser power based on the transmitted light grey value of each individual grain. Every 100 analyses were bracketed by a 4-acetamidophenol standard (see Lünsdorf et al., 2019, for further details).

Acquired spectra were automatically corrected for a temporal drift; smoothed, scaled, and corrected for the epoxy embedding medium spectrum; and compared to a modified version of the RRUFF database (Lafuente et al., 2015), and a hit index (Rodriguez et al., 2011) was assigned (Lünsdorf et al., 2019). Mineral assignments for spectra showing a hit index < 0.15 (good hits) were directly accepted, except clinopyroxene–orthopyroxene and amphibole–phyllosilicate which were re-examined due to potential confusion with each other. All assignments giving a hit index of 0.15–0.30 were re-examined to ensure correctness, and those giving a hit index of > 0.30 were screened for occasional spectra that still showed characteristic Raman bands, enabling an unequivocal mineral identification. All grains that could not be assigned to a specific mineral but show a transmitted light value similar to or lower than opaque minerals within the sample are grouped as "opaque". All remaining analyses are evaluated as "not identified".

In addition to mineral identification, clinopyroxene and olivine compositions were estimated based on Raman band positions following Wang et al. (2001), Kuebler et al. (2006), and Breitenfeld et al. (2018). Band positions of drift-corrected spectra were determined using iterative curve fitting (Lünsdorf and Lünsdorf, 2016). Fitting parameters include a spectral window of 200–1200 cm^{-1}, a linear baseline, and pseudo-Voigt functions.

3.2.2 Hyperspectral imaging of inclusion-bearing garnet

Garnet grains of the mounted heavy-mineral separates were examined for mineral inclusions by transmitted-light microscopy. Grains containing at least one inclusion $> 2\,\mu m$ in size were mapped in three dimensions by hyperspectral Raman imaging using a WITec alpha300R fibre-coupled ultrahigh-throughput spectrometer. Before analysis, the system was calibrated using an integrated Xe–Hg light source. The experimental setup included a 532 nm excitation laser, an automatically controlled laser output power of 30 mW, a 300 lines mm^{-1} grating covering a spectral range of 60–3900 cm^{-1} at a spectral resolution of $\sim 2.7\,cm^{-1}$, a 100× long-working-distance objective (NA 0.75), an acquisition time of 20 ms per spectrum, and a signal amplification by an electron-multiplying charge-coupled device. Spectra were collected in a 2 µm spaced three-dimensional grid (x–y–z) covering the full x–y extent of the individual grains and a depth (z direction) of 40 µm at maximum. Automated cosmic ray correction, background subtraction, spectral averaging/smoothing, and principal component analysis were performed using the WITec Project software. This method enables the confident identification of most inclusions $\geq 4\,\mu m$, as well as smaller inclusions for strong Raman scattering phases like quartz, coesite, rutile, and diamond (Schönig et al., 2022).

3.3 Electron microprobe analysis

The chemical composition of inclusion-bearing garnet grains was analysed using a JEOL JXA 8900 RL electron microprobe and a JEOL JXA-iHP200F, both equipped with five wavelength-dispersive spectrometers. Samples were coated with carbon to ensure conductivity. Measurement conditions include an accelerating voltage of 15 kV and a beam current of 20 nA. Counting times were 15 s for Si, Mg, Ca, Fe, and Al and 30 s for Ti, Cr, and Mn. Two measurement spots were set for each grain, one at the centre and one at the rim.

In addition to compositional evaluation based on molar proportions, the multivariate random forest classification scheme of Schönig et al. (2021b) was used to predict the original host rocks of detrital garnets regarding setting (either metamorphic, igneous, mantle, or metasomatic rocks; estimated classification success $> 95\,\%$), bulk-rock composition (either intermediate–felsic–sedimentary, mafic, ultramafic, alkaline, or calc-silicate rocks; estimated classification success $> 93\,\%$), and metamorphic conditions (either blueschist–greenschist, amphibolite, eclogite–ultrahigh-pressure, or granulite facies; estimated classification success $> 84\,\%$). Notably, although discrimination success rates are high (Schönig et al., 2021b), such predictions are not devoid of misclassifications and should be seen as a statistical tool, which becomes particularly powerful when integrated with inclusion analysis.

4 Results

4.1 Heavy-mineral assemblages

All monomineralic mineral grains of the mounted heavy-mineral concentrates of the 63–125, 125–250, and 250–500 µm grain-size fractions from each of the eight samples (Fig. 2) have been analysed by semi-automated Raman spectroscopy. This comprises a total of 66 301 grains, whereby 56 280 are potential transparent heavy minerals, and 52 130 of these (∼ 93 %) could be assigned to a specific mineral group (see Table S1 in the Supplement). On average, the heavy-mineral spectra of the individual samples for the 63–125, 125–250, and 250–500 µm fractions include ∼ 3536, ∼ 1674, and 1307 grains, respectively. The number of identified heavy minerals for the individual grain-size fractions and samples ranges between 424 grains for the 250–500 µm fraction of sample JS-NGO-03s and 4036 grains for the 63–125 µm fraction of JS-NGO-09s (Fig. 3).

In all samples, amphibole, garnet, orthopyroxene, and augitic clinopyroxene (see Fig. S1 in the Supplement) represent the majority of heavy minerals (Fig. 3). Considering the mean proportion of all individual samples and grain-size fractions, amphibole accounts for ∼ 39 %, garnet for ∼ 20 %, orthopyroxene for ∼ 16 %, and augitic clinopyroxene for ∼ 15 %. Sillimanite and apatite occur in smaller but substantial amounts of ∼ 5 % and ∼ 2 %, respectively. Accessory minerals comprise rutile (0.54 %), TiO_2 phases other than rutile (anatase, brookite, as well as intergrown polycrystals of anatase ± brookite ± rutile, 0.51 %), epidote-group minerals (0.48 %), titanite (0.29 %), forsteritic olivine (0.22 %; see Fig. S2 in the Supplement), zircon (0.11 %), monazite (0.09 %), tourmaline (0.04 %), spinel (0.04 %), prehnite (0.03 %), rhodonite (0.01 %), kyanite (< 0.01 %), staurolite (< 0.01 %), and chloritoid (< 0.01 %). While rutile, TiO_2 phases other than rutile, epidote-group minerals, titanite, olivine, zircon, and monazite occur in all samples but not all grain-size fractions, other accessories are restricted to a subset of samples. Notably, kyanite solely occurs in the 63–125 µm fraction of JS-NGO-17s ($n = 3$), staurolite solely occurs in the 63–125 µm fraction of JS-NGO-11s ($n = 1$), and chloritoid solely occurs in the 63–125 µm fraction of JS-NGO-01s ($n = 1$).

Although heavy-mineral assemblages of the individual samples show similar patterns, relative abundances are distinct. Sample JS-NGO-03s differs from all other samples by a comparatively high garnet and low augitic clinopyroxene content (Fig. 4a). In addition, this sample contains the highest amount of rutile, other TiO_2 phases, and monazite (Fig. 3). Samples JS-NGO-16s and JS-NGO-18s are characterised by a high proportion of sillimanite compared to orthopyroxene (Fig. 4a), as well as a low apatite content (Fig. 3). A similarly low apatite content is observed in JS-NGO-17s, which also shows increased but less pronounced sillimanite/orthopyroxene. Apart from that, the highest amount of titanite and tourmaline occurs in JS-NGO-17s. The other four samples, i.e. JS-NGO-01s, JS-NGO-09s, JS-NGO-11s, and JS-NGO-21s, are best discriminated considering garnet–amphibole and clinopyroxene–epidote ratios, with JS-NGO-09s and JS-NGO-21s showing the highest values for both and JS-NGO-01s showing the lowest value for the latter (Fig. 4b). Notably, variations with grain size are not related to hydrodynamic factors. For example, comparatively dense garnet is expected to be depleted over less dense amphibole and apatite with increasing grain size, a feature not observed here (Fig. 4c).

4.2 Garnet major-element composition

Compositional variations between analysed centres ($n = 2416$) and rims ($n = 2416$) of the inclusion-bearing garnet grains are minor, with > 98 % showing a difference of < 10 % for X_{Fe}, X_{Mg}, X_{Ca}, and X_{Mn} (molar proportions, see Fig. S3 in the Supplement; see Table S2 in the Supplement for the entire dataset). Considering the centre–rim mean composition, two populations can be distinguished: one very prominent, which comprises ∼ 85 % of the garnet grains, all showing X_{Ca} < 13 % and three-quarters showing X_{Ca} < 5 %, and one less pronounced population with X_{Ca} > 13 % (Fig. 5a). Both populations are characterised by low X_{Mn} contents but occasionally reach up to 35 % X_{Mn}, similar to the ultrahigh-pressure garnets proposed by Glassley et al. (2014).

Although virtually inseparable by considering only three oxides at a time (Fig. 5a), multivariate consideration of all pair-wise ratios of the eight analysed major oxides after Schönig et al. (2021b) indicates several subpopulations (Fig. 5b). The majority of the detrital garnets (∼ 78.3 %) are compositionally similar to garnet grown at granulite-facies conditions in an intermediate–felsic–sedimentary protolith. Smaller but substantial proportions are predicted to be sourced from intermediate–felsic–sedimentary amphibolite-facies rocks (∼ 7.0 %) and mafic amphibolite- (∼ 4.1 %), eclogite- (∼ 5.6 %), and granulite-facies rocks (∼ 2.0 %). In addition, ∼ 1.2 % and ∼ 1.0 % of the garnets are assigned to intermediate–felsic–sedimentary and mafic blueschist–greenschist-facies sources, respectively. Rarely, garnet resembles intermediate–felsic–sedimentary eclogite-facies rocks (∼ 0.4 %), intermediate–felsic igneous rocks (∼ 0.2 %), and metasomatic calc-silicate rocks (< 0.1 %).

Metamorphic garnets of intermediate–felsic–sedimentary and mafic affinity and of all metamorphic facies occur in all samples (Fig. 5c). However, pronounced differences in terms of relative proportions between individual samples as well as grain-size fractions are observed. On average, the amount of garnet from mafic protoliths is highest in JS-NGO-01s, JS-NGO-17s, and JS-NGO-21s, and in all samples mafic garnet decreases with increasing grain size compared to intermediate–felsic–sedimentary garnet (Fig. 6a). This trend is accompanied by an increase in granulite-facies

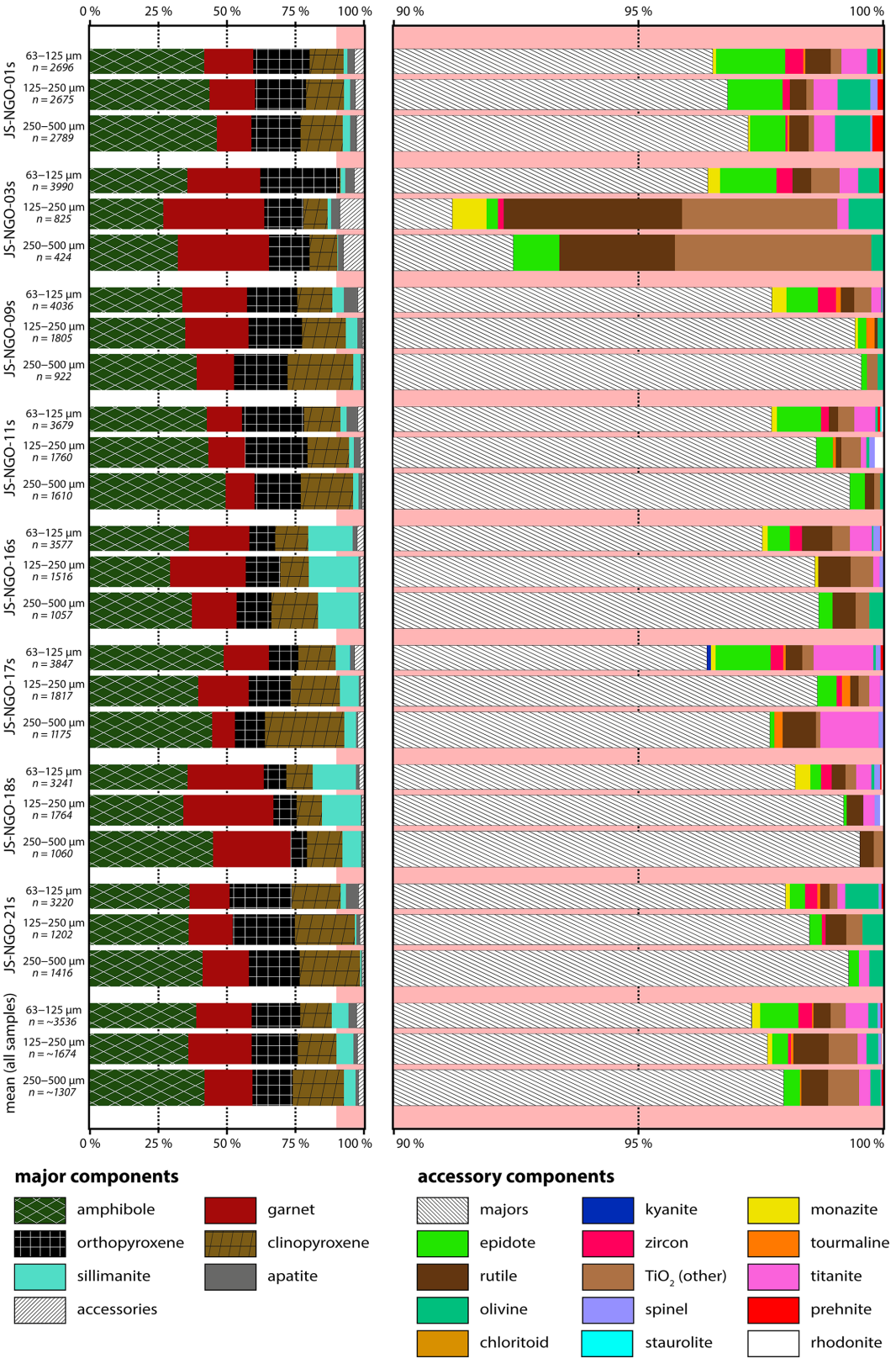

Figure 3. Heavy-mineral assemblages of the individual grains-size fractions of the individual samples. Accessory components are shown separately on an enlarged scale (90 %–100 %). Dataset given in Table S1 in the Supplement.

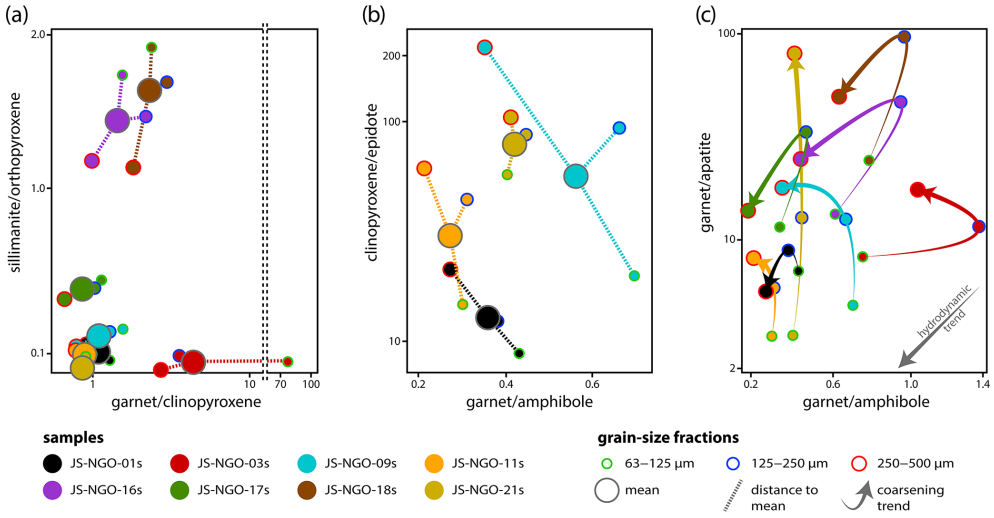

Figure 4. Inter- and intrasample variability in relative heavy-mineral proportions expressed by ratios. Panels **(a)** and **(b)** show grain-size fraction means for individual samples (connected to individual grain-size fractions by dashed lines), whereby **(b)** shows solely JS-NGO-01s, JS-NGO-09s, JS-NGO-11s, and JS-NGO-21s, which show minor separation in **(a)**. **(c)** Trends of increasing grain size for the individual samples (arrows) for comparatively dense garnet to less-dense amphibole and apatite. Dataset given in Table S1 in the Supplement.

garnet, which shows the highest proportions in JS-NGO-09s, JS-NGO-16s, and JS-NGO-18s. The decrease in granulite-facies garnet from 125–250 to 250–500 µm for JS-NGO-11s is related to the increasing amount of amphibolite-facies garnet (Fig. 5c). Inversely to an increase in granulite-facies and intermediate–felsic–sedimentary garnet, the proportion of blueschist–greenschist- and eclogite–ultrahigh-pressure-facies garnet decreases with increasing grain size (Fig. 6b). The highest amount of eclogite–ultrahigh-pressure-facies garnet occurs in JS-NGO-17s, and the highest amount of blueschist–greenschist-facies garnet occurs in JS-NGO-21s.

4.3 Mineral inclusions in garnet

A total of 11 165 garnet grains have been screened to reach a total number of 2416 inclusion-bearing garnet grains and ∼ 100 grains for each grain-size fraction of the individual samples (Table 1). Inclusion-bearing garnets have been analysed by three-dimensional hyperspectral Raman imaging, comprising a total of ∼ 685 million spectra (see Table S2 in the Supplement). Considering the mean of all grain-size fractions and samples, sillimanite is the most common inclusion type in terms of abundance, followed by quartz, rutile, zircon, graphite, phyllosilicates (mainly phlogopite–biotite, minor muscovite–paragonite, and chlorite), titanium oxides other than rutile, carbonates, opaque minerals (ilmenite, hematite, pyrite, and not identified phases), apatite, hydrous aluminium phases (mainly dickite, minor boehmite, and diaspore), fluid inclusions, amphibole, plagioclase, augitic clinopyroxene, and melt inclusions (Table 1). In addition, monazite, xenotime, alkali feldspar, titanite, orthopyroxene, epidote, and staurolite occur in < 1 % of the analysed garnets.

Garnets predicted to be sourced from blueschist–greenschist-, amphibolite-, eclogite–ultrahigh-pressure-facies rocks, as well as mafic granulite-facies metamorphic rocks, are subordinate compared to the dominance of intermediate–felsic–sedimentary granulite-facies garnet (Fig. 5c). The number of observations from these garnets has been increased in order to enable comparison of mineral inclusion types and major-element composition. For this purpose, the 125–250 µm grain-size fractions of samples JS-NGO-01s, JS-NGO-17s, and JS-NGO-21s have been chosen. The choice of the 125–250 µm fraction was a practical decision to compromise between the 250–500 µm fraction, which shows the highest proportion of inclusion-bearing garnets but the lowest amounts of garnets assigned to classes other than intermediate–felsic–sedimentary granulite facies, and the 63–125 µm fraction, which shows the lowest proportion of inclusion-bearing garnets but the highest amounts of garnets assigned to classes other than intermediate–felsic–sedimentary granulite facies (see Table 1 and Fig. 5c). Samples JS-NGO-01s, JS-NGO-17s, and JS-NGO-21s have been chosen because these show the highest proportion of garnets assigned to mafic and blueschist–greenschist and eclogite–ultrahigh-pressure sources, particularly in the 125–250 µm fraction (Fig. 6). From the three samples, a total of 5242 garnet grains were picked. Grains were efficiently pre-filtered by semi-quantitative compositional scanning using energy-dispersive X-ray spectroscopy, and only grains which are comparatively low in X_{Mg} and high in X_{Ca} and/or X_{Mn} were selected for further analysis (see Fig. S4 in the Supplement). The selected 570 grains were analysed by quantitative wavelength-dispersive spectroscopy using an electron microprobe, and only grains

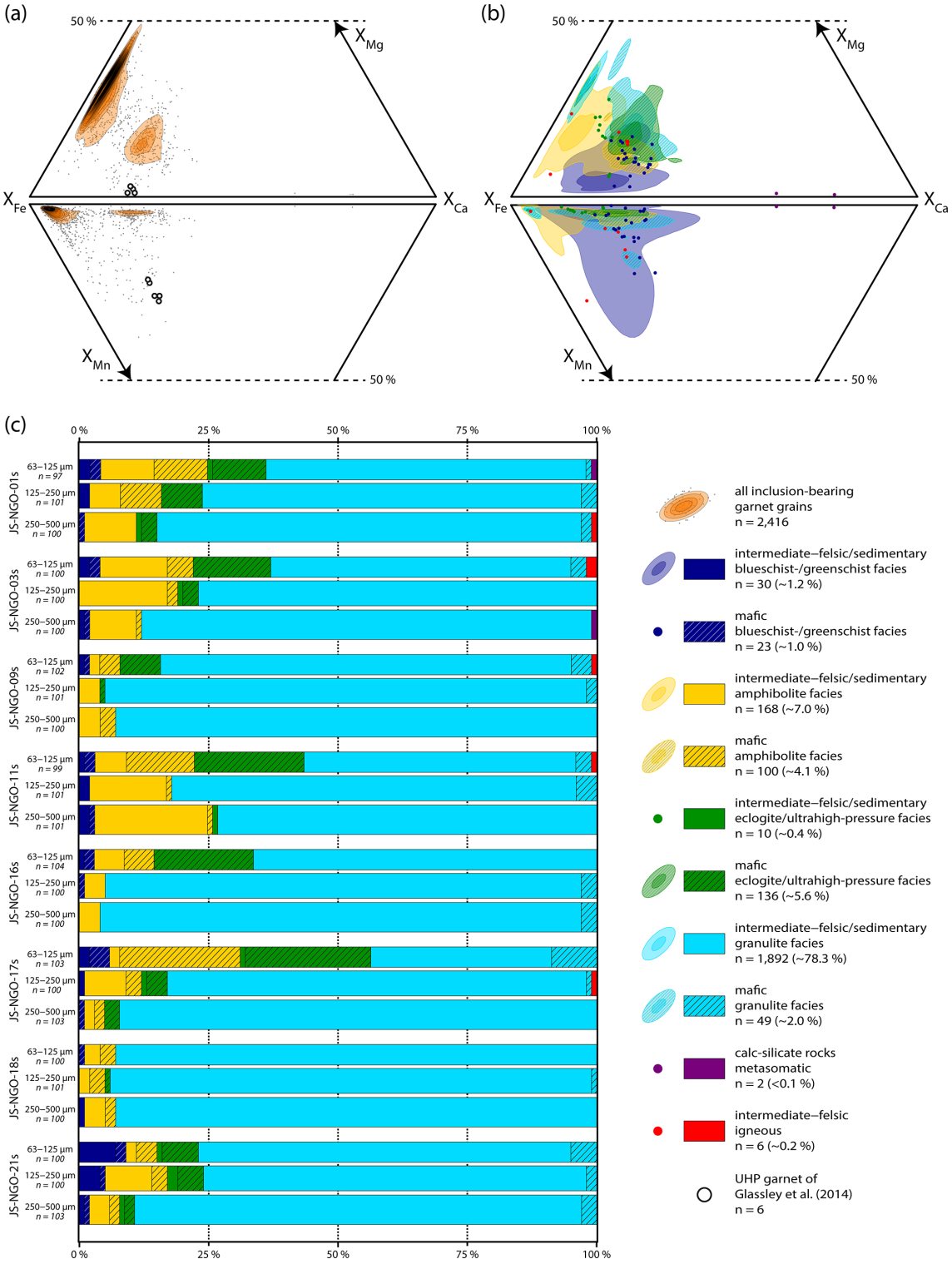

Figure 5. Garnet major-element composition. **(a)** Average core–rim composition of all inclusion-bearing garnets expressed in $X_{Fe}-X_{Mg}-X_{Ca}$ and $X_{Fe}-X_{Mn}-X_{Ca}$ ternary plots (see Fig. S3 in the Supplement for centre–rim variations) and shown as a kernel density map. For comparison, the composition of garnet from proposed ultramafic ultrahigh-pressure rocks is shown (Glassley et al., 2014). **(b)** Composition of garnets predicted to be derived from different host rocks after Schönig et al. (2021b) for data shown in **(a)**. **(c)** Bar plots showing the proportions of garnets assigned to different host rocks indicated in **(b)** for individual grain-size fractions of the individual samples. Dataset given in Table S2 in the Supplement.

https://doi.org/10.5194/ejm-35-479-2023

Table 1. Summary of mineral inclusion assemblages. Garnet grains containing specific inclusion types are given as percentages and ordered in decreasing abundance. Other inclusion types correspond to those that occur in < 1 % of all garnets. Percentage for all grain-size fractions is expressed as mean. Abbreviations: vfs – very fine sand (63–125 µm), fs – fine sand (125–250 µm), ms – medium sand (250–500 µm), Grt – garnet, Inc. – inclusion-bearing, Sil – sillimanite, Qz – quartz, Rt – rutile, Zrn – zircon, Gr – graphite, Phl–Bt – phlogopite–biotite, Ms–Pg – muscovite–paragonite, Chl – chlorite, Ant – anatase, Br – brookite, Psb – pseudobrookite, Cb – carbonates, Opq – opaque, Ap – apatite, Dck – dickite, Bhm – boehmite, Dsp – diaspore, FI – fluid inclusions (primary), Amp – amphibole, Pl – plagioclase, Cpx – clinopyroxene (augite), MI – melt inclusions, Mnz – monazite, Xtm – xenotime, Opx – orthopyroxene, Ep – epidote-group minerals, Ttn – titanite, Afs – alkali feldspar, and St – staurolite.

Sample (JS-NGO-)	Grain-size	Grt (*n*)	Inc. Grt (*n*/%)	Spectra ($n \times 10^6$)	Sil	Qz	Rt	Zrn	Gr	Phl–Bt + Ms–Pg + Chl	Ant + Br + Psb	Cb	Opq	Ap	Dck + Bhm + Dsp	FI	Amp	Pl	Cpx	MI	Others
01s	vfs	675	97/14	3.8	25	35	15	6	9	6	4	11	10	8	6	7	5	1	5	0	Mnz, Xtm
01s	fs	604	101/17	15.3	31	34	20	12	7	5	8	9	4	8	2	1	5	3	3	1	Opx, Ep, Ttn, Xtm
01s	ms	402	100/25	34.0	36	37	19	14	18	10	10	16	5	5	1	1	2	1	1	1	Afs, Opx, Mnz
03s	vfs	1349	100/7	2.6	21	44	9	3	8	10	0	6	3	5	2	4	0	2	5	0	Afs, Mnz
03s	fs	642	100/36	25.3	14	43	9	8	12	12	3	7	6	6	1	5	1	5	1	0	Mnz, Xtm
03s	ms	280	102/24	68.6	20	41	17	12	14	20	8	11	5	3	2	5	0	7	0	1	Mnz
09s	vfs	424	101/34	3.1	48	20	11	5	4	6	0	2	2	4	13	1	4	0	1	2	Ttn
09s	fs	297	100/63	18.0	62	18	12	7	7	6	7	2	6	0	6	1	0	2	0	0	Afs
09s	ms	160	99/16	61.5	48	34	30	18	13	18	12	7	7	3	4	2	2	1	0	3	Mnz, Xtm
11s	vfs	617	101/23	3.3	29	30	15	3	3	7	3	8	12	7	2	5	4	3	4	1	Afs
11s	fs	444	101/37	19.8	35	27	15	9	18	11	5	7	9	11	5	2	0	0	0	1	Xtm
11s	ms	274	104/16	59.6	26	33	14	26	16	11	8	12	12	11	1	1	3	1	0	0	St, Mnz
16s	vfs	639	100/26	2.7	48	24	7	7	3	5	3	3	4	4	7	3	1	4	1	0	Mnz, Xtm
16s	fs	379	100/36	20.4	62	12	11	14	4	0	11	8	7	2	5	0	0	0	0	1	–
16s	ms	276	103/18	70.5	59	24	24	20	17	5	8	6	3	7	2	2	1	0	0	2	Mnz
17s	vfs	575	100/25	2.7	22	50	9	8	4	7	1	7	4	7	3	2	3	3	2	0	Afs, Ttn
17s	fs	395	103/37	19.2	54	23	15	6	7	5	7	9	7	3	6	3	0	2	2	1	Afs
17s	ms	275	100/18	71.5	38	37	21	27	13	15	11	3	5	11	5	1	1	0	2	3	Mnz
18s	vfs	566	101/25	5.2	63	14	11	11	7	2	9	1	2	0	2	1	1	0	0	0	–
18s	fs	401	100/25	18.2	66	16	11	14	5	0	6	0	4	3	6	0	1	0	0	0	Mnz
18s	ms	271	100/37	58.8	59	25	24	16	7	13	12	5	1	3	5	0	1	0	0	3	Ep, Xtm
21s	vfs	588	100/17	4.1	40	27	13	7	6	5	4	2	5	7	10	1	1	3	2	1	Afs
21s	fs	352	100/28	30.0	28	32	19	21	7	3	8	8	6	7	4	7	1	1	1	1	Xtm
21s	ms	280	103/37	66.8	36	38	25	19	10	12	14	9	3	7	3	2	3	1	0	4	Ep, Mnz
01s	all	1681	298/19	53.1	30	35	18	11	11	7	7	12	6	7	3	3	4	2	3	1	Afs, Opx, Ep, Ttn, Mnz, Xtm
03s	all	2271	300/20	96.5	18	43	12	8	11	14	4	8	5	5	2	5	0	5	2	0	Afs, Mnz, Xtm
09s	all	881	303/40	82.6	53	24	18	10	8	10	6	4	5	2	8	1	2	1	0	2	Afs, Ttn, Mnz, Xtm
11s	all	1335	301/25	82.7	30	30	15	13	12	10	5	9	11	10	3	3	2	1	1	1	Afs, St, Mnz, Xtm
16s	all	1294	304/26	93.6	56	20	14	14	8	3	7	6	5	4	5	2	1	1	0	1	Mnz, Xtm
17s	all	1245	306/27	93.4	38	37	15	14	8	9	6	6	5	7	5	2	1	2	2	1	Afs, Ttn, Mnz
18s	all	1238	301/27	82.2	63	18	15	14	6	5	9	2	2	2	4	0	1	0	0	1	Ep, Mnz, Xtm
21s	all	1220	303/27	100.9	35	32	19	16	8	7	9	6	5	7	6	3	2	2	1	2	Afs, Ep, Mnz, Xtm
all	all	11 165	2416/26	684.9	40	30	16	12	9	8	7	7	5	5	4	2	2	2	1	1	Afs, Opx, Ep, Ttn, Mnz, Xtm

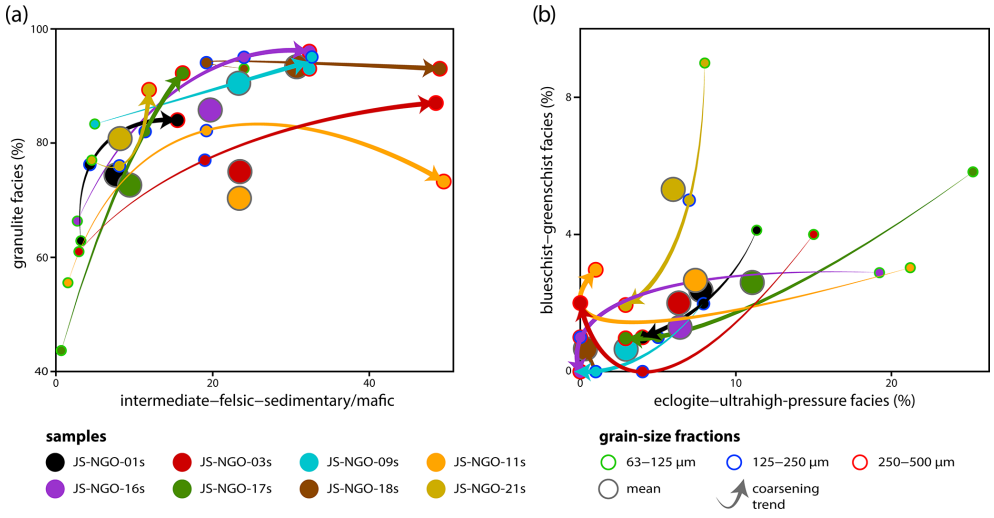

Figure 6. Inter- and intrasample variability and trends of increasing grain size for garnets assigned to individual host rocks after Schönig et al. (2021b). Shown are grain-size means for individual samples (either host-rock proportions or ratios) connected by a coarsening-oriented arrow, as well as sample means. Dataset given in Table S2 in the Supplement.

that are not assigned to an intermediate–felsic–sedimentary granulite-facies source ($n = 520$) have been investigated for mineral inclusion types. From the 520 grains, 253 contain inclusions $> 2\,\mu m$, whereby 7, 57, 38, and 57 are assigned to a mafic blueschist–greenschist-, amphibolite-, granulite-, and eclogite–ultrahigh-pressure-facies source and 24, 61, and 9 to an intermediate–felsic–sedimentary blueschist–greenschist-, amphibolite-, and eclogite–ultrahigh-pressure-facies source, respectively (see Table S3 in the Supplement).

Sillimanite, the most common inclusion type (Table 1), is very abundant in garnet predicted to be sourced from intermediate–felsic–sedimentary protoliths, particularly those of granulite facies, whereas sillimanite is almost absent in garnet from mafic protoliths (Fig. 7). Typically, sillimanite inclusions are needle-shaped and occur in high numbers within single grains. Whenever the needles are exposed at garnet surfaces, these are either replaced by dickite (rarely boehmite and diaspore) or lost (e.g. Fig. 8a). In addition to sillimanite, melt inclusions are also mainly observed in intermediate–felsic–sedimentary garnet, but for those of granulite facies no protolith preference exists, and melt inclusions are absent in blueschist–greenschist-facies garnet (Fig. 7). The melt inclusions show negative crystal shapes and are polyphase, consisting of various assemblages of SiO_2 polymorphs (quartz/cristobalite/tridymite), $(K,Na)AlSi_3O_8$ polymorphs (kokchetavite/kumdykolite), and hydrous phases (phlogopite–biotite/muscovite–paragonite/amphibole) and sometimes additionally containing carbonate and/or apatite and/or low-grade carbonaceous matter (e.g. Fig. 8b; see also remarks in Tables S2 and S3 in the Supplement). Although less pronounced than sillimanite and melt inclusions, graphite preferentially occurs in intermediate–felsic–sedimentary garnet (Fig. 7). Notably, two types of graphite are observed: one occurs in polyphase melt and secondary fluid inclusions (see below), and the second one occurs as monophase inclusions. While the first type shows variable ordering and maturity, the monophase type always shows a triperiodic (well-ordered and mature) structure (see Fig. S5 in the Supplement; Cancado et al., 2008; Rantitsch et al., 2016).

In contrast to sillimanite, melt, and graphite, inclusions of amphibole, plagioclase, and clinopyroxene are much more abundant in garnet predicted to originate from mafic metamorphic rocks (Fig. 7). Inclusions of clinopyroxene are exclusively augitic and are most frequent in mafic eclogite–ultrahigh-pressure-facies garnet (e.g. Fig. S6a in the Supplement). Raman band positions imply a slightly higher content of Mg in clinopyroxene inclusions in garnet assigned to eclogite–ultrahigh-pressure- and granulite-facies sources compared to those of amphibolite facies (see Fig. S1 in the Supplement). Amphibole and plagioclase are instead most common in mafic amphibolite-facies garnet. Notably, neither amphibole nor augitic clinopyroxene occurs in blueschist–greenschist-classified garnet.

On average, inclusions of quartz, apatite, zircon, phlogopite–biotite, rutile, and fluids do not show a strong tendency to be more common in garnet of either mafic or intermediate–felsic–sedimentary affinity. However, especially apatite and fluid inclusions, as well as subordinately quartz, are much less frequent in intermediate–felsic–sedimentary granulite-facies garnet compared to those assigned to a mafic protolith (Fig. 7). Furthermore, rutile inclusions are remarkably enriched in eclogite–ultrahigh-pressure- and granulite-facies garnet and sometimes oriented (Fig. 8c), while phlogopite–biotite is much more frequent

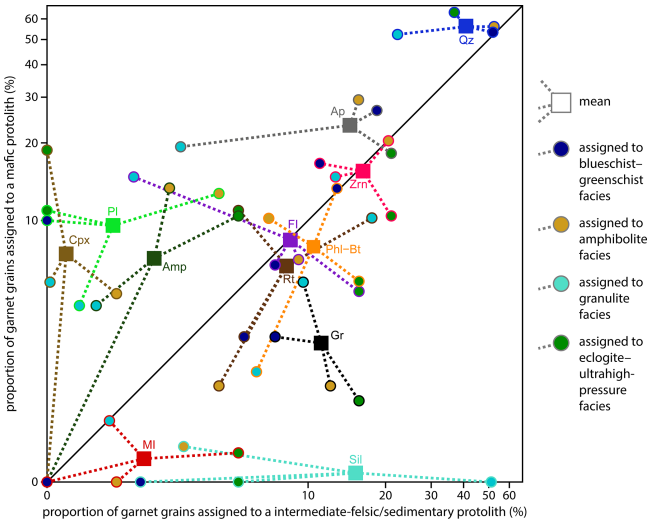

Figure 7. Proportions of garnets containing specific inclusion types as a function of classification based on major elements after Schönig et al. (2021b). Predictions for host-rock composition are given on the axes, and individual data points are shown for the mean, as well as the different metamorphic-facies types. Zero values are preserved without applying the logarithmic transformation. Abbreviations: Amp – amphibole, Ap – apatite, Cpx – clinopyroxene (augitic), FI – primary fluid inclusion, Gr – graphite, MI – melt inclusion, Phl–Bt – phlogopite–biotite, Pl – plagioclase, Qz – quartz, Rt – rutile, Sil – sillimanite, and Zrn – zircon. Datasets are given in Table S2 and S3 in the Supplement.

in blueschist–greenschist-facies garnet (e.g. Fig. S6b in the Supplement), particularly compared to the low abundance in those assigned to granulite-facies conditions (Fig. 7). Quartz inclusions in garnet of all discrimination classes, including blueschist–greenschist facies, commonly show well-developed facets and edges (e.g. Fig. 8d). Some fluid inclusions (mainly consisting of carbon dioxide and carbonate) form linear trails crosscutting garnet grains, clearly implying a secondary origin, and are not considered here (Fig. 8e). Other fluid inclusions are isolated, show negative crystal shapes, and are often enriched along garnet growth zones, implying a primary origin, i.e. entrapment during garnet growth (Fig. 8f). These fluid inclusions are polyphase and consist of various assemblages including carbonate minerals, pyrophyllite, carbonaceous matter of variable maturity, carbon dioxide, and rarely methane (see also remarks in Tables S2 and S3 in the Supplement).

5 Discussion

5.1 Constraining the metamorphic framework

Both the occurrence of minerals of low chemical stability, particularly olivine (Fig. 3), and the non-hydrodynamic sorting of mineral species, especially the proportions of apatite and amphibole compared to garnet (Fig. 4c), show that the studied heavy-mineral assemblages represent first-order (fresh) erosional material from metamorphic rocks of the Nordre Strømfjord shear zone. Samples JS-NGO-16s and JS-NGO-18s, and to a lower extent JS-NGO-17s, show comparatively high sillimanite content, while all others show comparatively high orthopyroxene (Fig. 4a), agreeing with the higher abundance of para-metamorphic rocks in the former and ortho-metamorphic rocks in the latter. The lower sillimanite content in JS-NGO-17s compared to JS-NGO-16s and JS-NGO-18s is accompanied with a higher content of titanite (Fig. 3), as well as a much higher proportion of garnet predicted to be sourced from mafic lithologies (Fig. 5c). This implies that most erosional material of this sample is sourced from the mafic lenses close to the sampling location (Fig. 2). The tonalitic orthopyroxene gneiss, which covers the majority of catchment JS-NGO-03s (Fig. 2), sheds much lower amounts of augitic clinopyroxene but higher amounts of garnet (Fig. 4a). Overall, the heavy minerals faithfully represent the geological framework of the study area, showing that the modern sands comprise a naturally sampled mixture of erosional material.

With regard to metamorphic conditions, the abundance of sillimanite and orthopyroxene in the heavy-mineral assemblages calls for granulite-facies conditions, which particularly affected the large volumes of felsic rocks in the study area. This is supported by the dominance of garnet grains predicted to be grown at granulite-facies conditions in intermediate–felsic–sedimentary protoliths based on their major-element composition (Figs. 5c and 6a). The majority of those ($\sim 51\,\%$) contain sillimanite inclusions, and $\sim 18\,\%$ of these also contain rutile inclusions ($\sim 18\,\%$; Fig. 7), or reversely formulated, $\sim 40\,\%$ of the rutile-bearing garnets assigned to granulite-facies conditions also contain sillimanite. Considering the co-stability of rutile and sillimanite, this indicates granulite-facies metamorphism at medium to high pressure, interpreted here as representing peak-temperature conditions in the study area. This is well in agreement with thermobarometric constraints of 700–900 °C and 0.6–1.0 GPa for rocks of the central Nagssugtoqidian Orogen (Davidson, 1979; Hansen, 1979; Glassley, 1983; Fig. 2b). Melt inclusions comprising SiO_2 and $(K,Na)AlSi_3O_8$ polymorphs, as well as hydrous phases, also called nanogranitoids (e.g. Cesare et al., 2009, 2015; Ferrero et al., 2018; Fig. 8d), show that granulite-facies metamorphism was accompanied by partial melting and peritectic garnet growth. Both secondary fluid inclusions (Fig. 8e) and the replacement of sillimanite by hydrous aluminium phases for inclusions that were not isolated from the external metamorphic conditions by the host garnet (Fig. 8a) indicate high fluid activity following the granulite-facies peak. This agrees with the high proportions of amphibole in the heavy-mineral assemblages, as well as trace amounts of low-temperature phases like prehnite (Fig. 3), which probably represent matrix phases re-equilibrated during either retrograde metamorphism or a

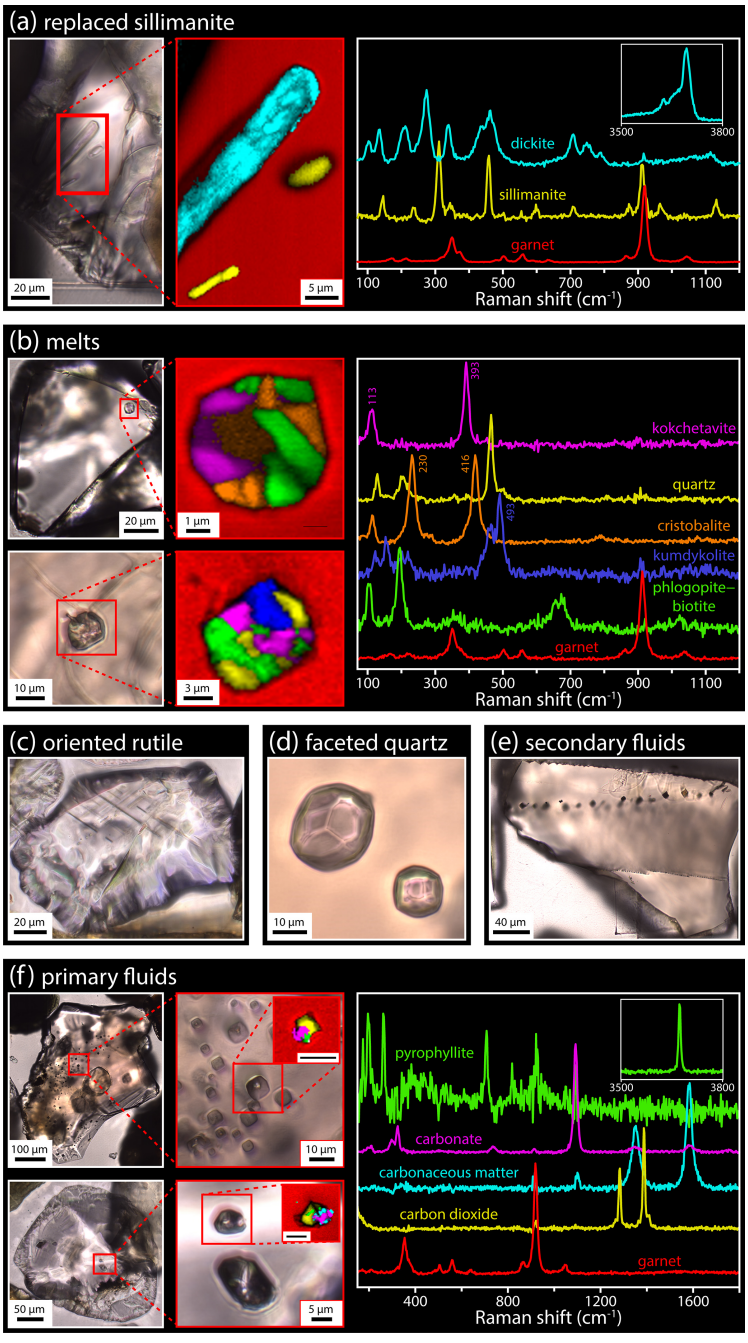

Figure 8. Photomicrographs and Raman images showing inclusion characteristics. **(a)** Garnet number 35 from the 63–125 µm fraction of JS-NGO-09s, which is predicted to be sourced from a granulite-facies rock of intermediate–felsic–sedimentary composition based on major-element discrimination after Schönig et al. (2021b). Shown are two isolated sillimanite inclusions and one similar needle-shaped inclusion of dickite which is exposed at the garnet surface in the lower left corner of the image. **(b)** Melt inclusions in garnet number 93 from the 63–125 µm fraction of JS-NGO-09s (upper) and number 78 from the 250–500 µm fraction of JS-NGO-21s (lower), predicted to be of granulite-facies intermediate–felsic–sedimentary and mafic origin, respectively. **(c)** Oriented rutile inclusions in garnet number 24 from the 63–125 µm fraction of JS-NGO-21s, predicted to be sourced from a granulite-facies rock of intermediate–felsic–sedimentary composition. **(d)** Quartz inclusions showing well-developed facets and edges in garnet number 66 of the picked and chemically pre-screened garnets from the 125–250 µm fraction of sample JS-NGO-21s, predicted to be sourced from a blueschist–greenschist-facies rock. **(e)** Fluid inclusions of secondary origin forming a linear trail through the host garnet. Garnet number 172 of the picked and chemically pre-screened garnets from the 125–250 µm fraction of sample JS-NGO-21s, predicted to be of amphibolite-facies intermediate–felsic–sedimentary origin. **(f)** Primary polyphase fluid inclusions showing a negative shape in garnet number 58 from the 250–500 µm fraction of JS-NGO-09s (upper) and garnet number 52 from the 125–250 µm fraction of sample JS-NGO-21s (lower), both predicted to be sourced from granulite-facies rocks of intermediate–felsic–sedimentary composition. Datasets are given in Tables S2 and S3 in the Supplement.

subsequent event like the post-collisional large-scale folding and/or strike-slip shearing (Connelly et al., 2000; van Gool et al., 2002).

Although the granulite-facies peak and following retrograde/subsequent metamorphism seem to have pervasively overprinted the preceding metamorphic history, trace amounts of kyanite in the heavy-mineral assemblage of JS-NGO-17s point to a metamorphic stage either at higher pressure or at similar pressure but lower temperature (Fig. 3). This is corroborated by the much lower but considerable proportions of garnets predicted to originate from blueschist–greenschist- ($\sim 2.2\,\%$), amphibolite- ($\sim 11.1\,\%$), and eclogite–ultrahigh-pressure-facies rocks ($\sim 6.0\,\%$). Of particular interest are those of blueschist–greenschist and eclogite–ultrahigh-pressure facies, which have the potential to constrain conditions for the low-temperature and high-pressure part of the metamorphic cycle, respectively. The observation of well-developed facets and edges for quartz inclusions in both garnet types is probably the result of inclusion shape modification at higher temperatures (after entrapment) to reduce the surface energy of the host-inclusion system (Cesare et al., 2021; Fig. 8d) and thus implies prograde garnet growth. This is further supported by the high maturity of carbonaceous matter (i.e. large proportions of triperiodic graphite) in garnets of all observed compositions, including those predicted to be of blueschist–greenschist-facies origin (see Fig. S5 in the Supplement). The occurrence of a single band at $\sim 1580\,\mathrm{cm}^{-1}$ (G band) and splitting of the higher-frequency band at $\sim 2700\,\mathrm{cm}^{-1}$ indicate that they were exposed to temperature conditions in excess of 600 °C (e.g. Lespade et al., 1984; Beyssac et al., 2002, 2003), likely after initial growth. Post-entrapment modification during cooling from high temperatures can also explain the polyphase character of primary fluid inclusions with negative crystal shape (Fig. 8f). Particularly the high concentrations of Al and Ca required to precipitate pyrophyllite and carbonate, which are far above common concentrations in simple COH fluids, imply cation exchange between the primary fluid and the host garnet as a natural consequence of cooling (Carvalho et al., 2020).

Regarding the prograde path, the blueschist–greenschist-classified garnets are compositionally different from all other garnets, mainly due to their high Mn content (Fig. 5b). A discrimination of a potential blueschist- or greenschist-facies origin based on garnet major-element chemistry is ambiguous without further information regarding bulk-rock composition. However, these garnets show markedly different mineral inclusion assemblages with a considerably higher proportion of phyllosilicates (mainly phlogopite–biotite, e.g. Fig. S6b in the Supplement) and an absence of melt, amphibole, and augitic clinopyroxene inclusions (Fig. 7). As any type of blueschist-facies-indicative minerals is absent (i.e. sodium-rich amphiboles, chloritoid, aragonite, and/or lawsonite) and phlogopite–biotite is extremely scarce in blueschist-facies rocks due to the replacement by white mica, stilpnomelane, and/or amphibole (e.g. Brown, 1975; Bucher and Frey, 2002), the occurrence of phlogopite–biotite inclusions calls for greenschist-facies conditions. Garnet growth under such low-temperature and low-pressure conditions is not the norm, but the garnet stability field shifts to lower temperature and pressure for Mn-rich protoliths (e.g. Atherton, 1964; White et al., 2014). Mn-rich rocks in the studied catchments are recorded by trace amounts of rhodonite in the heavy-mineral assemblages (Fig. 3), and their occurrence is also in accordance with reported ultramafic rocks from the study area which contain $\sim 7\,\mathrm{wt}\,\%$ MnO (Glassley et al., 2014).

Garnets assigned to the eclogite–ultrahigh-pressure-facies conditions are mainly predicted to be derived from mafic rocks (Fig. 5c). Notably, classification rates (correct classification/(correct classification + misclassification) × 100) for host-rock composition are higher ($> 93\,\%$) than for metamorphic facies ($> 84\,\%$). Particularly amphibolite- and granulite-facies garnets that equilibrated at pressures $> 1.0\,\mathrm{GPa}$ are more prone to be misclassified (Schönig et al., 2021b). This is obvious for the detrital garnets assigned to eclogite–ultrahigh-pressure facies in this study, which show high compositional overlaps with global occurrences of mafic amphibolite-, granulite-, and eclogite–ultrahigh-pressure-facies garnets (Fig. 9a). When considering mafic garnets equilibrated at pressures $\geq 2.1\,\mathrm{GPa}$ and those equilibrated at pressures between 1.0 and 2.1 GPa separately, the detrital grains of this study are comparatively more similar to the latter (Fig. 9b). This agrees with predictions using the multivariate garnet discrimination scheme of Tolosana-Delgado et al. (2018), which gives roughly similar probabilities for an amphibolite-, granulite-, and eclogite-facies source rock (see Fig. S7 in the Supplement). An origin from metamorphic rocks $< 2.1\,\mathrm{GPa}$ is also more compatible with their inclusion assemblages, which show abundant augitic clinopyroxene without any indication of a sodium component (see Fig. S1 in the Supplement), as well as the occurrence of amphibole and plagioclase (Figs. 7 and S6b in the Supplement). If these would have grown at pressure conditions above the amphibolite-to-eclogite or granulite-to-eclogite transition, a breakdown of albite to form jadeite + quartz would be expected (e.g. Holland, 1980).

Overall, the detrital record is most consistent with a prograde metamorphic history starting at greenschist–amphibolite-facies conditions and evolving through the amphibolite facies to a pressure maximum at the transition between amphibolite-, granulite-, and eclogite-facies conditions. Despite all reasonable efforts given by the acquisition of such a large dataset, not a single observation has been made that hints to either ultrahigh-pressure conditions or conditions deeply within the eclogite facies. Following the pressure maximum, a temperature maximum was reached at medium- to high-pressure granulite-facies conditions accompanied by partial melting, strongly overprinting and blurring the preceding evolution. Fluids were present during the pro-

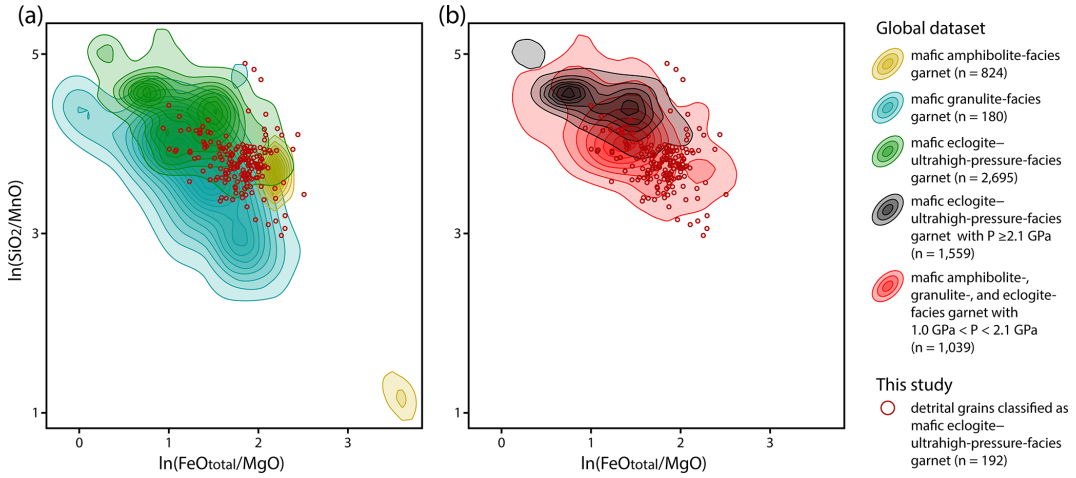

Figure 9. Composition of detrital garnets classified as being sourced from mafic eclogite–ultrahigh-pressure rocks compared to a global dataset after Schönig et al. (2021b). Panel **(a)** shows compositional overlaps of the detrital grains with mafic amphibolite-, granulite-, and eclogite–ultrahigh-pressure garnets. Panel **(b)** shows the detrital grains compared to mafic garnets that equilibrated at pressures ≥ 2.1 GPa and those equilibrated at pressures of 1.0–2.1 GPa. Datasets are given in Tables S2 and S3 in the Supplement.

grade path and during retrograde metamorphism and/or a subsequent event following the temperature maximum. Such a metamorphic evolution is consistent with a subduction–collision regime involving crustal thickening at intermediate gradients $> 600\,^{\circ}\mathrm{C\,GPa^{-1}}$ (e.g. Brown, 2007). This is well in agreement with decades-long work in the Nagssugtoqidian Orogen (see Sect. 2), as well as the dominant geodynamic regime in the Paleoproterozoic (see Fig. 1), but in strong contrast to modern-style plate tectonics involving deep, cold subduction and the extreme ultrahigh-pressure conditions at thermal gradients $< 150\,^{\circ}\mathrm{C\,GPa^{-1}}$ as proposed by Glassley et al. (2014).

5.2 Reappraisal of ultrahigh-pressure indicators

The pressure–temperature estimates proposed by Glassley et al. (2014) are based on microstructures interpreted as exsolution and inclusions of carbonaceous matter interpreted as remnant diamond. Generally, proving the exsolution origin of crystallographic orientation relationships is not straightforward and requires careful acquisition and interpretation of orientation data (e.g. Axler and Ague, 2015; Griffiths et al., 2020; Keller and Ague, 2022). Glassley et al. (2014), however, solely provide optical and microscopic observations. In addition, such crystallographic orientation relationships may also be produced by other processes than exsolution, for example, by oriented interface nucleation (Griffiths et al., 2020).

The interpretation of a precursor ahrensite (Fe_2SiO_4) based on oriented quartz inclusions by Glassley et al. (2014, 2016) can only be evaluated as speculative due to the lack of any comparable reports. Occurrences of oriented rutile inclusions in garnet of a quartzo-feldspathic rock, which have also been observed in detrital garnets (Fig. 8c), are interpreted by Glassley et al. (2014) as exsolution due to exhumation from ultrahigh-pressure metamorphic conditions. However, oriented rutile inclusions in garnet have been frequently reported from rocks that never underwent ultrahigh-pressure metamorphism (see Fig. 1 in Keller and Ague, 2020). Temperature and melt composition are more important for titanium solubility in garnet than pressure (e.g. Ackerson et al., 2017). Better evidence for ultrahigh-pressure conditions is the exsolution of orthopyroxene requiring a majoritic precursor (e.g. Haggerty and Sautter, 1990), as interpreted by Glassley et al. (2014) for oriented inclusions in garnet from the ultramafic rocks. These inclusions are described as rhombohedral in shape, consisting of "finely intergrown mats of Cl-bearing hydrous phases" showing some scatter in their major-element composition, and reconstruction of an anhydrous composition matches with orthopyroxene, interpreted as being altered to the hydrous phase (Glassley et al., 2014). This description raises several uncertainties and inconsistencies. First, exsolved orthopyroxene inclusions in garnet commonly show a needle/lamellae or octagonal/hexagonal shape depending on orientation, making a rhombohedral shape anomalous (Haggerty and Sautter, 1990; van Roermund and Drury, 1998; van Roermund et al., 2000; Ye et al., 2000; Song et al., 2004). Second, the described intergrowth and their compositional scatter indicate a polycrystalline character, questioning whether single phases or polyphases have been analysed and whether an average composition allows the reconstruction of an anhydrous orthopyroxene composition. Third, the hydration of precursor orthopyroxene inclusions requires fluid infiltration. This seems unlikely for all inclusions which are usually shielded from the external metamorphic conditions by the host garnet, particularly when considering (1) that orthopyroxene is preserved in the rock

matrix and (2) that "exceptionally low a_{H_2O} during decompression and cooling" is specified by Glassley et al. (2014) to explain the preservation of ultrahigh-pressure assemblages.

With regard to diamond, the reported spectra do not show a sharp Raman band at $\sim 1332\,cm^{-1}$ (see Fig. 8 of Glassley et al., 2014), which is of first-order significance for diamond identification (e.g. Krishnan, 1945). By contrast, the spectra of Glassley et al. (2014) only show very broad intensity maxima of $\sim 100\,cm^{-1}$ width occurring in the frequency region of diamond, accompanied by a general spectral pattern characteristic of very low-grade carbonaceous matter. In addition, intensity maxima also occur outside the frequency region of carbonaceous material at > 1800 and $< 1250\,cm^{-1}$. Similar wavy spectral patterns are typically artefacts introduced by broad-band emissions resulting in intensity variations due to the individual instrument response function, which includes wavelength-variable grating efficiency, detector quantum efficiency, and filter transmission (e.g. Fryling et al., 1993). Broad-band emissions acquired during Raman spectroscopy are commonly the result of sampling a material that fluoresces at the excitation laser wavelength or sampling light from other broad-band emitters located in the lab, like white lamps. Furthermore, the spectra reported by Glassley et al. (2014) show a sharp band at 1100–1150 cm^{-1} described to be related to the garnet background, but garnet does not show vibrations at this frequency. Potential sources of this band can be manifold, including the presence of an additional undescribed phase or even spectral lines from noble gases like those found in lamps. In any case, the absence of a characteristic diamond Raman band and the presence of artefacts do not permit the spectra of Glassley et al. (2014) to be interpreted as being related to remnant diamond inclusions.

6 Conclusions

A statistically based approach has been applied to screen the Nordre Strømfjord shear zone in the Paleoproterozoic Nagssugtoqidian Orogen of Greenland for ultrahigh-pressure rock occurrences and to constrain metamorphic boundary conditions, which is particularly feasible within single tectonometamorphic units. From eight modern sands representing naturally mixed erosional material from metamorphic rocks of the area, a total of 52 130 detrital heavy minerals have been assigned to a specific mineral group, and major-element chemistry and mineral inclusion assemblages of 2669 garnet grains – filtered from a total of 16 407 – have been acquired. Although being less precise for individual garnets compared to common approaches of metamorphic petrology due to the virtually lost paragenetic context, the integration of detrital garnet chemistry and mineral inclusions allows for reasonable constraints on the metamorphic evolution of an area on a larger scale by a comparatively low number of samples.

The majority of garnet in the Nordre Strømfjord shear zone formed during a temperature peak at medium- to high-pressure granulite-facies conditions accompanied by partial melting, as recorded by the co-existence of sillimanite and rutile inclusions and the occurrence of melt inclusions. Before reaching peak temperature, metamorphic rocks evolved on a prograde path starting at greenschist-facies conditions via the upper amphibolite facies through a pressure peak at the transition between amphibolite-, granulite-, and eclogite-facies conditions. The greenschist-facies part is recorded by garnets being unique in composition, lacking common amphibolite-facies inclusions but containing phlogopite–biotite inclusions. By contrast, amphibolite-facies garnets often contain amphibole, augitic clinopyroxene, and plagioclase inclusions, all of which are also present in garnets that crystallised at the pressure peak as implied by their chemical composition. The absence of a sodium component in augitic clinopyroxene inclusions and the presence of plagioclase show that peak pressure garnets did not equilibrate deeply within eclogite-facies conditions. These boundary conditions match with a common Barrovian-type metamorphic path during the Paleoproterozoic subduction–collision event.

Considering (1) the reconstructed metamorphic boundary conditions, (2) the absence of any low-temperature–high-pressure and ultrahigh-pressure minerals in our notably large detrital dataset, and (3) the vulnerability of previously proposed "evidence" for ultrahigh-pressure conditions, we conclude that the Nordre Strømfjord shear zone does not record a Paleoproterozoic modern-style plate-tectonic regime involving cold and deep subduction.

Data availability. All data derived from this research are presented in the enclosed tables, figures, and Supplement.

Supplement. The supplement related to this article is available online at: https://doi.org/10.5194/ejm-35-479-2023-supplement.

Author contributions. JS: conceptualisation, fieldwork, formal analysis, investigation, visualisation, software, writing – original draft. CB: formal analysis, investigation, writing – review and editing. GM: conceptualisation, fieldwork, funding acquisition, writing – review and editing. HvE: conceptualisation, funding acquisition, writing – review and editing. NKL: software, writing – review and editing.

Competing interests. The contact author has declared that none of the authors has any competing interests.

Disclaimer. Publisher's note: Copernicus Publications remains neutral with regard to jurisdictional claims in published maps and institutional affiliations.

Special issue statement. This article is part of the special issue "Probing the Earth: Melt and solid inclusions as probes to understand nature". It is not associated with a conference.

Acknowledgements. We thank the Government of Greenland and the Mineral Licence and Safety Authority for information and permission supporting our research (scientific survey licence no. SP-35/2020). Sirius Greenland APS is thanked for support in logistics. We gratefully acknowledge the use of equipment in the Göttingen laboratory for correlative Light and Electron Microscopy (GoeLEM – http://www.mineralogie.uni-goettingen.de, last access: 8 June 2023) at the University of Göttingen and the lab support by Andreas Kronz, Jochen Gätjen, Dominik Sorger, and Antje Grebe. Reviews by Richard Palin and an anonymous referee and editorial handling by Silvio Ferrero are gratefully acknowledged.

Financial support. This research has been supported by the Deutsche Forschungsgemeinschaft (grant no. EY23/27-1).

This open-access publication was funded
by the University of Göttingen.

Review statement. This paper was edited by Silvio Ferrero and reviewed by Richard Palin and one anonymous referee.

References

Ackerson, M. R., Watson, E. B., Tailby, N. D., and Spear, F. S.: Experimental investigation into the substitution mechanisms and solubility of Ti in garnet, Am. Mineral., 102, 158–172, https://doi.org/10.2138/am-2017-5632, 2017.

Atherton, M. P.: The garnet isograd in pelitic rocks and its relationship to metamorphic facies, Am. Mineral., 49, 1331–1349, 1964.

Axler, J. A. and Ague, J. J.: Oriented multiphase needles in garnet from ultrahigh-temperature granulites, Connecticut, USA, Am. Mineral., 100, 2254–2271, https://doi.org/10.2138/am-2015-5018, 2015.

Bak, J., Korstgård, J., and Sørensen, K.: A major shear zone within the Nagssugtoqidian of West Greenland, Tectonophysics, 27, 191–209, https://doi.org/10.1016/0040-1951(75)90016-5, 1975.

Baldwin, S. L., Schönig, J., Gonzalez, J. P., Davies, H., and von Eynatten, H.: Garnet sand reveals rock recycling processes in the youngest exhumed high- and ultrahigh-pressure terrane on Earth, P. Natl. Acad. Sci. USA, 118, e2017231118, https://doi.org/10.1073/pnas.2017231118, 2021.

Beyssac, O., Goffé, B., Chopin, C., and Rouzaud, J. N.: Raman spectra of carbonaceous material in metasediments: a new geothermometer, J. Metamorph. Geol., 20, 859–871, https://doi.org/10.1046/j.1525-1314.2002.00408.x, 859–871, 2002.

Beyssac, O., Goffé, B., Petitet, J. P., Froigneux, E., Moreau, M., and Rouzaud, J. N.: On the characterization of disordered and heterogeneous carbonaceous materials by Raman spectroscopy, Spectrochim. Acta A, 59, 2267–2276, https://doi.org/10.1016/S1386-1425(03)00070-2, 2003.

Breitenfeld, L. B., Dyar, M. D., Carey, C. J., Tague Jr, T. J., Wang, P., Mullen, T., and Parente, M.: Predicting olivine composition using Raman spectroscopy through band shift and multivariate analyses, Am. Mineral., 103, 1827–1836, https://doi.org/10.2138/am-2018-6291, 2018.

Brown, E. H.: A Petrogenetic Grid for Reactions Producing Biotite and other Al–Fe–Mg Silicates in the Greenschist Facies, J. Petrol., 16, 258–271, https://doi.org/10.1093/petrology/16.2.258, 1975.

Brown, M.: Duality of thermal regimes is the distinctive characteristic of plate tectonics since the Neoarchean, Geology, 34, 961–964, https://doi.org/10.1130/G22853A.1, 2006.

Brown, M.: Metamorphic conditions in orogenic belts: a record of secular change, Int. Geol. Rev., 49, 193–234, https://doi.org/10.2747/0020-6814.49.3.193, 2007.

Brown, M. and Johnson, T.: Secular change in metamorphism and the onset of global plate tectonics, Am. Mineral., 103, 181–196, https://doi.org/10.2138/am-2018-6166, 2018.

Brown, M. and Johnson, T.: Metamorphism and the evolution of subduction on Earth, Am. Mineral., 104, 1065–1082, https://doi.org/10.2138/am-2019-6956, 2019.

Brown, M., Johnson, T., and Gardiner, N. J.: Plate tectonics and the Archean Earth, Annu. Rev. Earth Planet. Sci., 48, 291–320, https://doi.org/10.1146/annurev-earth-081619-052705, 2020.

Bucher, K. and Frey, M.: Petrogenesis of Metamorphic Rocks, Springer-Verlag, Berlin-Heidelberg, ISBN 978-3-662-04916-7, 2002.

Cancado, L. G., Takai, K., Enoki, T., Endo, M., Kim, Y. A., Mizusaki, H., Speziali, N. L., Jorio, A., and Pimenta, M. A.: Measuring the degree of stacking order in graphite by Raman spectroscopy, Carbon, 46, 272–275, https://doi.org/10.1016/j.carbon.2007.11.015, 2008.

Carvalho, B. B., Bartoli, O., Cesare, B., Tacchetto, T., Gianola, O., Ferri, F., Aradi, L. E., and Szabó, C.: Primary CO_2-bearing fluid inclusions in granulitic garnet usually do not survive, Earth Planet. Sc. Lett., 536, 116170, https://doi.org/10.1016/j.epsl.2020.116170, 2020.

Cawood, P. A., Hawkesworth, C. J., and Dhuime, B.: The continental record and the generation of continental crust, Geol. Soc. Am. Bull., 125, 14–32, https://doi.org/10.1130/B30722.1, 2013.

Cesare, B., Ferrero, S., Salvioli-Mariani, E., Pedron, D., and Cavallo, A.: "Nanogranite" and glassy inclusions: The anatectic melt in migmatites and granulites, Geology, 37, 627–630, https://doi.org/10.1130/G25759A.1, 2009.

Cesare, B., Acosta-Vigil, A., Bartoli, O., and Ferrero, S.: What can we learn from melt inclusions in migmatites and granulites?, Lithos, 239, 186–216, https://doi.org/10.1016/j.lithos.2015.09.028, 2015.

Cesare, B., Parisatto, M., Mancini, L., Peruzzo, L., Franceschi, M., Tacchetto, T., Reddy, S., Spiess, R., Nestola, F., and Marone, F.: Mineral inclusions are not immutable: Evidence of post-entrapment thermally-induced shape change of quartz in garnet, Earth Planet. Sc. Lett., 555, 116708, https://doi.org/10.1016/j.epsl.2020.116708, 2021.

Cleveland, W. S., Grosse, E., and Shyu, W. M.: Local regression models, in: Statistical Models in S, edited by: Chambers, J. M. and Hastie, T. J., Wadsworth and Brooks/Cole, Springer-Verlag, New York, https://doi.org/10.1201/9780203738535, 1992.

Connelly J. N. and Mengel F. C.: Evolution of Archean components in the Paleoproterozoic Nagssugtoqidian orogen, West Greenland, Geol. Soc. Am. Bull., 112, 747–763, https://doi.org/10.1130/0016-7606(2000)112<747:EOACIT>2.0.CO;2, 2000.

Connelly J. N., van Gool J. A. M., and Mengel F. C.: Temporal evolution of a deeply eroded orogen: the Nagssugtoqidian Orogen, West Greenland, Can. J. Earth Sci., 37, 1121–1142, https://doi.org/10.1139/e00-032, 2000.

Davidson, L. M.: Nagssugtoqidian granulite facies metamorphism in the Holsteinsborg region, West Greenland, Rapport Grønlands Geologiske Undersøgelse, 89, 97–108, https://doi.org/10.34194/rapggu.v89.7570, 1979.

de Oliveira Chaves, A. and Porcher, C. C.: Petrology, geochemistry and Sm-Nd systematics of the Paleoproterozoic Itaguara retroeclogite from São Francisco/Congo Craton: one of the oldest records of the modern-style plate tectonics, Gondwana Res., 87, 224–237, https://doi.org/10.1016/j.gr.2020.06.014, 2020.

Dhuime, B., Hawkesworth, C. J., Cawood, P. A., and Storey, C. D.: A change in the geodynamics of continental growth 3 billion years ago, Science, 335, 1334–1336, https://doi.org/10.1126/science.1216066, 2012.

Escher, J. C. and Pulvertaft, T. C. R.: 1995. Geological map of Greenland, 1 : 2, 500, 000, Geological Survey of Greenland, Copenhagen, https://collections.lib.uwm.edu/digital/collection/agdm/id/8475/ (last access: 11 July 2023), 1995.

Ferrero, S., Godard, G., Palmeri, R., Wunder, B., and Cesare, B.: Partial melting of ultramafic granulites from Dronning Maud Land, Antarctica: Constraints from melt inclusions and thermodynamic modelling, Am. Mineral., 103, 610–622, https://doi.org/10.2138/am-2018-6214, 2018.

Fleet, W. F.: Petrological notes on the Old Red Sandstone of the West Midlands, Geol. Mag., 63, 505–516, https://doi.org/10.1017/S0016756800085484, 1926.

Forsyth, D. and Uyeda, S.: On the relative importance of the driving forces of plate motion, Geophys. J. Int., 43, 163–200, https://doi.org/10.1111/j.1365-246X.1975.tb00631.x, 1975.

François, C., Debaille, V., Paquette, J. L., Baudet, D., and Javaux, E. J.: The earliest evidence for modern-style plate tectonics recorded by HP–LT metamorphism in the Paleoproterozoic of the Democratic Republic of the Congo, Sci. Rep., 8, 15452, https://doi.org/10.1038/s41598-018-33823-y, 2018.

Fryling, M., Frank, C. J., and McCreery, R. L.: Intensity calibration and sensitivity comparisons for CCD/Raman spectrometers, Appl. Spectrosc., 47, 1965–1974, 1993.

Ganade, C. E., Rubatto, D., Lanari, P., Hermann, J., Tesser, L. R., and Caby, R.: Fast exhumation of Earth's earliest ultrahigh-pressure rocks in the West Gondwana orogen, Mali, Geology, 51, 647–651, https://doi.org/10.1130/G50998.1, 2023.

Ganne, J., De Andrade, V., Weinberg, R. F., Vidal, O., Dubacq, B., Kagambega, N., Naba, S., Baratoux, L., Jessell, M., and Allibon, J.: Modern-style plate subduction preserved in the Palaeoproterozoic West African craton, Nat. Geosci., 5, 60–65, https://doi.org/10.1038/ngeo1321, 2012.

Glassley, W. E.: Deep crustal carbonates as CO_2 fluid sources: evidence from metasomatic reaction zones, Contrib. Mineral. Petrol., 84, 15–24, https://doi.org/10.1007/BF01132326, 1983.

Glassley, W. E. and Sørensen, K.: Constant P_S-T amphibolite to granulite facies transition in Agto (West Greenland) metadolerites: implications and applications, J. Petrol., 21, 69–105, https://doi.org/10.1093/petrology/21.1.69, 1980.

Glassley W. E., Korstgård J. A., and Sørensen K.: Two tectonically significant enclaves in the Nordre Strømfjord shear zone at Ataneq, central West Greenland, Geol. Surv. Denmark Greenland Bull., 13, 49–52, https://doi.org/10.34194/geusb.v13.4974, 2007.

Glassley W. E., Korstgård J. A., and Sørensen K.: K-rich brine and chemical modification of the crust during continent–continent collision, Nagssugtoqidian Orogen, West Greenland, Precambrian Res., 180, 47–62, https://doi.org/10.1016/j.precamres.2010.02.020, 2010.

Glassley, W. E., Korstgård, J. A., Sørensen, K., and Platou, S. W.: A new UHP metamorphic complex in the ∼ 1.8 Ga Nagssugtoqidian Orogen of West Greenland, Am. Mineral., 99, 1315–1334, https://doi.org/10.2138/am.2014.4726, 2014.

Glassley, W. E., Korstgård, J. A., and Sørensen, K.: Further observations related to a possible occurrence of terrestrial ahrensite, Am. Mineral., 101, 2347–2350, https://doi.org/10.2138/am-2016-5899, 2016.

Griffiths, T. A., Habler, G., and Abart, R.: Determining the origin of inclusions in garnet: challenges and new diagnostic criteria, Am. J. Sci., 320, 753–789, https://doi.org/10.2475/11.2020.01, 2020.

Haggerty, S. E. and Sautter, V.: Ultradeep (greater than 300 kilometers), ultramafic upper mantle xenoliths, Science, 248, 993–996, https://doi.org/10.1126/science.248.4958.993, 1990.

Hansen, B. F.: Some charnockitic rocks in the Nagssugtoqidian of West Greenland, Rapport Grønlands Geologiske Undersøgelse, 89, 85–96, https://doi.org/10.34194/rapggu.v89.7569, 1979.

Hawkesworth, C. J., Cawood, P. A., and Dhuime, B.: Tectonics and crustal evolution, GSA Today, 26, 4–11, https://doi.org/10.1130/GSATG272A.1, 2016.

Holder, R. M., Viete, D. R., Brown, M., and Johnson, T. E.: Metamorphism and the evolution of plate tectonics, Nature, 572, 378–381, https://doi.org/10.1038/s41586-019-1462-2, 2019.

Holland, T. J.: The reaction albite = jadeite + quartz determined experimentally in the range 600–1200 °C, Am. Mineral., 65, 129–134, 1980.

Jahn, B. M., Caby, R., and Monie, P.: The oldest UHP eclogites of the World: age of UHP metamorphism, nature of protoliths and tectonic implications, Chem. Geol., 178, 143–158, https://doi.org/10.1016/S0009-2541(01)00264-9, 2001.

Kalsbeek, F. and Nutman, A. P.: Anatomy of the Early Proterozoic Nagssugtoqidian orogen, West Greenland, explored by reconnaissance SHRIMP U-Pb zircon dating, Geology, 24, 515–518, https://doi.org/10.1130/0091-7613(1996)024<0515:AOTEPN>2.3.CO;2, 1996.

Kalsbeek, F., Pidgeon, R. T., and Taylor, P. N.: Nagssugtoqidian mobile belt of West Greenland: a cryptic 1850 Ma suture between two Archaean continents – chemical and isotopic evidence, Earth Planet. Sc. Lett., 85, 365–385, https://doi.org/10.1016/0012-821X(87)90134-8, 1987.

Katayama, I. and Maruyama, S.: Inclusion study in zircon from ultrahigh-pressure metamorphic rocks in the Kokchetav massif: an excellent tracer of metamorphic history, J. Geol. Soc. Lond., 166, 783–796, https://doi.org/10.1144/0016-76492008-019, 2009.

Keller, D. S. and Ague, J. J.: Quartz, mica, and amphibole exsolution from majoritic garnet reveals ultra-deep sedi-

ment subduction, Appalachian orogen, Sci. Adv., 6, eaay5178, https://doi.org/10.1126/sciadv.aay51, 2020.

Keller, D. S. and Ague, J. J.: Predicting and explaining crystallographic orientation relationships of exsolved precipitates in garnet using the edge-to-edge matching model, J. Metamorph. Geol., 40, 1189–1218, https://doi.org/10.1111/jmg.12662, 2022.

Krishnan, R. S.: Raman spectrum of diamond, Nature, 155, 171–171, https://doi.org/10.1038/155171a0, 1945.

Kuebler, K. E., Jolliff, B. L., Wang, A., and Haskin, L. A.: Extracting olivine (Fo–Fa) compositions from Raman spectral peak positions, Geochim. Cosmochim. Ac., 70, 6201–6222, https://doi.org/10.1016/j.gca.2006.07.035, 2006.

Lafuente, B., Downs, R. T., Yang, H., Stone, N.: The power of databases: The RRUFF project, in: Highlights in Mineralogical Crystallography, edited by: Armbruster, T. and Danisi, R. M., De Gruyter, Berlin, 1–30, ISBN 978-3-11-041704-3, 2015.

Lespade, P., Marchand, A., Couzi, M., and Cruege, F.: Caracterisation de materiaux carbones par microspectrometrie Raman, Carbon, 22, 375–385, https://doi.org/10.1016/0008-6223(84)90009-5, 1984.

Lünsdorf, N. K. and Lünsdorf, J. O., 2016: Evaluating Raman spectra of carbonaceous matter by automated, iterative curve-fitting, Int. J. Coal Geol., 160, 51–62, https://doi.org/10.1016/j.coal.2016.04.008, 2016.

Lünsdorf, N. K., Kalies, J., Ahlers, P., Dunkl, I., and von Eynatten, H.: Semi-automated heavy-mineral analysis by Raman spectroscopy, Minerals, 9, 385, https://doi.org/10.3390/min9070385, 2019.

Marker, M., Mengel, F., and Van Gool, J.: Evolution of the Palaeoproterozoic Nagssugtoqidian orogen: DLC investigations in West Greenland, Rapport Grønlands Geologiske Undersøgelse, 165, 100–105, https://doi.org/10.34194/rapggu.v165.8288, 1995.

Maruyama, S., Liou, J. G., and Terabayashi, M.: Blueschists and eclogites of the world and their exhumation, Int. Geol. Rev., 38, 485–594, https://doi.org/10.1080/00206819709465347, 1996.

Mazur, S., Anczkiewicz, R., Szczepański, J., van Gool, J. A. M., and Thirlwall M.: Palaeoproterozoic metamorphism and cooling of the northern Nagssugtoqidian orogen, West Greenland, Precambrian Res., 196, 171–192, https://doi.org/10.1016/j.precamres.2011.12.005, 2012.

McKenzie, D. and Parker, R.: The North Pacific: An Example of Tectonics on a Sphere, Nature, 216, 1276–1280, https://doi.org/10.1038/2161276a0, 1967.

Müller, S., Dziggel, A., Kolb, J., and Sindern, S.: Mineral textural evolution and PT-path of relict eclogite-facies rocks in the Paleoproterozoic Nagssugtoqidian Orogen, South-East Greenland, Lithos, 296, 212–232, https://doi.org/10.1016/j.lithos.2017.11.008, 2018.

Olesen, N. Ø.: Geological map of Greenland, 1 : 100, 000, sheet Agto 67 V.1 Nord, Geological Survey of Greenland, Copenhagen, 1984.

Palin, R. M., Santosh, M., Cao, W., Li, S. S., Hernández-Uribe, D., and Parsons, A.: Secular change and the onset of plate tectonics on Earth, Earth-Sci. Rev., 207, 103172, https://doi.org/10.1016/j.earscirev.2020.103172, 2020.

Perchuk, A. L. and Morgunova, A. A.: Variable P–T paths and HP-UHP metamorphism in a Precambrian terrane, Gridino, Russia: Petrological evidence and geodynamic implications, Gondwana Res., 25, 614–629, https://doi.org/10.1016/j.gr.2012.09.009, 2014.

Ramberg, H.: On the petrogenesis of the gneiss complexes between Sukkertoppen and Christianshaab, West Greenland, Meddelinger Dansk Geologisk Forening, 11, 312–327, 1948.

Rantitsch, G., Lämmerer, W., Fisslthaler, E., Mitsche, S., and Kaltenböck, H.: On the discrimination of semi-graphite and graphite by Raman spectroscopy, Int. J. Coal Geol., 159, 48–56, https://doi.org/10.1016/j.coal.2016.04.001, 2016.

R Core Team: R: a language and environment for statistical computing, R Foundation for Statistical Computing, Vienna, Austria, https://www.R-project.org/ (last access: 12 July 2021), 2021.

Rodriguez, J. D., Westenberger, B. J., Buhse, L. F., and Kauffman, J. F.: Quantitative evaluation of the sensitivity of library-based Raman spectral correlation methods, Anal. Chem., 83, 4061–4067, https://doi.org/10.1021/ac200040b, 2011.

Salminen, J., Elming, S. Å., and Layer, P.: Timing the breakup of the Baltica and Laurentia connection in Nuna – Rapid plate motion oscillation and plate tectonics in the Mesoproterozoic, Precambrian Res., 384, 106923, https://doi.org/10.1016/j.precamres.2022.106923, 2023.

Schönig, J., Meinhold, G., von Eynatten, H., and Lünsdorf, N. K.: Tracing ultrahigh-pressure metamorphism at the catchment scale, Sci. Rep., 8, 2931, https://doi.org/10.1038/s41598-018-21262-8, 2018a.

Schönig, J., Meinhold, G., von Eynatten, H., and Lünsdorf, N. K.: Provenance information recorded by mineral inclusions in detrital garnet, Sed. Geol., 376, 32–49, https://doi.org/10.1016/j.sedgeo.2018.07.009, 2018b.

Schönig, J., von Eynatten, H., Meinhold, G., and Lünsdorf, N. K.: Diamond and coesite inclusions in detrital garnet of the Saxonian Erzgebirge, Germany, Geology, 47, 715–718, https://doi.org/10.1130/G46253.1, 2019.

Schönig, J., von Eynatten, H., Meinhold, G., Lünsdorf, N. K., Willner, A. P., and Schulz, B.: Deep subduction of felsic rocks hosting UHP lenses in the central Saxonian Erzgebirge: Implications for UHP terrane exhumation, Gondwana Res., 87, 320–329, https://doi.org/10.1016/j.gr.2020.06.020, 2020.

Schönig, J., von Eynatten, H., Meinhold, G., and Lünsdorf, N. K.: Life-cycle analysis of coesite-bearing garnet, Geol. Mag., 158, 1421–1440, https://doi.org/10.1017/S0016756821000017, 2021a.

Schönig, J., von Eynatten, H., Tolosana-Delgado, R., and Meinhold, G.: Garnet major-element composition as an indicator of host-rock type: a machine learning approach using the random forest classifier, Contrib. Mineral. Petrol., 176, 98, https://doi.org/10.1007/s00410-021-01854-w, 2021b.

Schönig, J., von Eynatten, H., Meinhold, G., and Lünsdorf, N. K.: The sedimentary record of ultrahigh-pressure metamorphism: a perspective review, Earth-Sci. Rev., 227, 103985, https://doi.org/10.1016/j.earscirev.2022.103985, 2022.

Silverman, B. W.: Density Estimation for Statistics and Data Analysis, Chapman & Hall, London, https://doi.org/10.1007/978-1-4899-3324-9, 1986.

Song, S., Zhang, L., and Niu, Y.: Ultra-deep origin of garnet peridotite from the North Qaidam ultrahigh-pressure belt, Northern Tibetan Plateau, NW China, Am. Mineral., 89, 1330–1336, https://doi.org/10.2138/am-2004-8-922, 2004.

Stern, R. J.: The Orosirian (1800–2050 Ma) plate tectonic episode: Key for reconstructing the Proterozoic tectonic record, Geosci. Front., 14, 101553, https://doi.org/10.1016/j.gsf.2023.101553, 2023.

St-Onge, M. R., van Gool, J. A., Garde, A. A., and Scott, D. J.: Correlation of Archaean and Palaeoproterozoic units between northeastern Canada and western Greenland: constraining the pre-collisional upper plate accretionary history of the Trans-Hudson orogen, in: Earth Accretionary Systems in Space and Time, edited by: Cawood P. A. and Kröner A., Geol. Soc. Spec. Publ., 318, 193–235, https://doi.org/10.1144/SP318, 2009.

Taylor, P. N. and Kalsbeek, F.: Dating the metamorphism of Precambrian marbles: Examples from Proterozoic mobile belts in Greenland, Chem. Geol., 86, 21–28, https://doi.org/10.1016/0168-9622(90)90003-U, 1990.

Tolosana-Delgado, R., von Eynatten, H., Krippner, A., and Meinhold, G.: A multivariate discrimination scheme of detrital garnet chemistry for use in sedimentary provenance analysis, Sed. Geol., 375, 14–26, https://doi.org/10.1016/j.sedgeo.2017.11.003, 2018.

van Gool, J. A. M. and Marker, M.: Explanatory notes to the Geological map of Greenland, 1 : 100, 000, Ussuit 67 V.2 Nord, Geological Survey of Denmark and Greenland, Copenhagen, https://doi.org/10.34194/geusm.v3.4596, 2007.

van Gool, J. A. M., Connelly, J. N., Marker, M., and Mengel, F. C.: The Nagssugtoqidian Orogen of West Greenland: tectonic evolution and regional correlations from a West Greenland perspective, Can. J. Earth Sci., 39, 665–686, https://doi.org/10.1139/e02-027, 2002.

van Gool J. A. M., Kriegsman L. M., Marker M., and Nichols G. T.: Thrust stacking in the inner Nordre Strømfjord area, West Greenland: Significance for the tectonic evolution of the Palaeoproterozoic Nagssugtoqidian orogen, Precambrian Res., 93, 71–86, https://doi.org/10.1016/S0301-9268(98)00098-9, 1999.

van Roermund, H. L. M. and Drury, M. R.: Ultra-high pressure ($P > 6$ GPa) garnet peridotites in Western Norway: exhumation of mantle rocks from > 185 km depth, Terra Nova, 10, 295–301, https://doi.org/10.1046/j.1365-3121.1998.00213.x, 1998.

van Roermund, H. L. M., Drury, M. R., Barnhoorn, A., and de Ronde, A. A.: Super-silicic garnet microstructures from an orogenic garnet peridotite, evidence for an ultra-deep (> 6 GPa) origin, J. Metamorph. Geol., 18, 135–147, https://doi.org/10.1046/j.1525-1314.2000.00251.x, 2000.

Venables, W. N. and Ripley, B. D.: Modern Applied Statistics with S, Springer-Verlag, New York, https://doi.org/10.1007/978-0-387-21706-2, 2002.

Wang, A., Jolliff, B. L., Haskin, L. A., Kuebler, K. E., and Viskupic, K. M.: Characterization and comparison of structural and compositional features of planetary quadrilateral pyroxenes by Raman spectroscopy, Am. Mineral., 86, 790–806, https://doi.org/10.2138/am-2001-0703, 2001.

Weller, O. M. and St-Onge, M. R.: Record of modern-style plate tectonics in the Palaeoproterozoic Trans-Hudson orogen, Nat. Geosci., 10, 305–311, https://doi.org/10.1038/ngeo2904, 2017.

White, R. W., Powell, R., and Johnson, T. E.: The effect of Mn on mineral stability in metapelites revisited: New a–x relations for manganese-bearing minerals, J. Metamorph. Geol., 32, 809–828, https://doi.org/10.1111/jmg.12095, 2014.

Wickham, H.: ggplot2: Elegant Graphics for Data Analysis, Springer-Verlag, New York, ISBN 978-3-319-24277-4, https://ggplot2.tidyverse.org (last access: 19 June 2020), 2016.

Xu, C., Kynický, J., Song, W., Tao, R., Lü, Z., Li, Y., Yang, Y., Pohanka, M., Galiova, M. V., Zhang, L., and Fei, Y.: Cold deep subduction recorded by remnants of a Paleoproterozoic carbonated slab, Nat. Commun., 9, 2790, https://doi.org/10.1038/s41467-018-05140-5, 2018.

Ye, K., Cong, B., and Ye, D.: The possible subduction of continental material to depths greater than 200 km, Nature, 407, 734–736, https://doi.org/10.1038/35037566, 2000.